University of Bergen

Department of Physics and Technology

Analysis of 3D Pixel Detectors for the ATLAS Inner Tracker Upgrade

Andreas Løkken Heggelund

Master's Thesis in Experimental Particle Physics

June 2017

Abstract

The silicon 3D pixel detector represent a detector technology that has a higher radiation tolerance compared to the conventional planar pixel detectors. This detector technology is one of the technologies proposed to be installed in the new ATLAS Inner Tracker.

In this thesis an analysis of three such 3D pixel detectors has been performed on data collected at two testbeams in 2015 and 2016. The charge collection efficiency, tracking resolution and the active edge of the detectors have been investigated. Furthermore, a detailed Monte Carlo simulation of the full testbeam experiment has been performed.

A good efficiency and resolution was measured and full depletion was observed at 5V bias voltage. The results from the simulation was analysed and compared to the results from the testbeams.

Acknowlegdements

I would first like to thank my supervisor Professor Bjarne Stugu, for all the invaluable help and guidance he has given me through these last two years. I would also like to thank you for having given me the opportunity to travel across Europe to attend conferences and to participate in experiments at CERN. You have significantly increased my understanding and interest in particle physics.

Secondly, I would like to thank Dr. Zongchang Yang and Dr. Ole Røhne for their assistance and teachings during both of the extensive testbeams. Without you I would not have understood the first thing of what was going on. A special thanks to Dr. Yang for being an excellent travel companion and for answering my many trivial questions.

To all the people I have been so lucky to get to know at the University; Are Træet, Simen Hellesund, Lars Fredrik Fjæra, Steffen Mæland, Inga Strümke, Magne Lauritzen and Hans Heum, thank you for the many heated discussions and humorous moments. I have truly enjoyed them, and look forward to many more. I would especially like to thank Mr. Fjæra for proofreading my thesis and for commenting on every error he could find, no matter how small.

To my dear parents and brother I would like to direct my most sincere gratitude. Your unconditional belief in me means a lot to me, and for that I am forever grateful.

Finally I would like to thank my girlfriend Amalie Austrheim for her wonderful support and patience during my most stressful times, when I haven't been much around to do chores. You have the ability to always pick me up, and without you I would not have known the best of life.

Andreas Heggelund
Bergen, 30. Mai

Contents

Introduction

Motivation

In experiments studying particles emerging from high-energy collisions several detection systems are needed in order to measure all the properties of the particles. One of these detection systems is the tracking detector made up of silicon pixel and strip detectors, with the main purpose of measuring the ionization produced when charged particles pass through them. This is done in order to measure the momentum and direction of the particles, as well as to detect vertices where shortlived particles have decayed. Requirements on the placement of these detectors close to the collision point expose these detectors to a very high radiation dose that over time significantly reduces the properties of the material. Additionally, the occupancy in this region is extremely high so in order to resolve each particle track separately the detectors need a very precise and unambiguous resolution.

In 2026, the Large Hadron Collider (LHC) will be upgraded to the High Luminosity LHC (HL-LHC). This upgrade is planned to dramatically increase the luminosity[1] of the LHC, which imposes new challenges for the experiments along the accelerators circumference, as the radiation levels also will increase. In the ATLAS experiment the Inner Detector currently consists of planar and 3D silicon pixel detectors in addition to silicon strip detectors. This type of detectors are prone to reduced charge collection efficiencies and thus reduced tracking resolution when exposed to high radiation fluences. Therefore, a new Inner Tracker (ITk) is proposed where all layers consist of pixel and strip detectors with a higher radiation tolerance capable of withstanding the harsher environment close to the beam line [1].

One of the proposed detector technologies for the ITk is the silicon 3D pixel detector. These detectors are distinguished from the planar pixel detectors by their electrode configuration. Instead of having electrodes implanted on the top and bottom of a silicon wafer, the 3D pixel detectors have electrode columns vertically etched into the sensor bulk. This enables a complete separation of the depletion

[1]The concept of luminosity is explained in section 3.1.1.

depth and the sensor thickness, in addition to enabling much shorter inter-electrode distances. Shorter electrode separations represents shorter drift times for the charge carriers and thus an increased radiation hardness as well as a reduced operation voltage.

Structure of the thesis

This thesis is focused on an analysis of three silicon 3D pixel detector prototypes, fabricated at SINTEF Microsystems and Nanotechnology Laboratory (MiNaLab), that were tested in two test beams at CERN in 2015/16. The detectors under investigation consist of 80×336 pixels that measure 250×50 μm with an electrode separation of 67 μm. Additionally, the 3D geometry of these detectors eliminate the need of a guard-ring in the detectors circumference enabling the fabrication of a so-called active edge. This active edge is an extension of the active area of the sensor beyond its nominal edge and increases the active area of the detectors.

The second part of this thesis is focused on a full Monte Carlo simulation of the test beam experiment and comparison to real data. The detailed detector simulation help us understand properties we might not have seen in the real data. Additionally, the simulations give us insight into aspects such as how multiple scattering and other material effects influence our measurements. With this knowledge various cuts can be performed on the acceptance of tracks in the analysis.

The first chapter give an introduction to the physics of semiconductor devices and a more detailed description of planar and 3D pixel detectors. Furthermore, theory of detector physics and radiation deterioration of detectors is provided. In the second chapter signal acquisition is described as well as the theory of energy deposition by charged particles in thin layer of material. The third chapter give an overview of the LHC and the ATLAS experiment. Here concepts such as luminosity and cross-section is explained.

Moving on to the fourth chapter, an introduction to the test beam activities, and an overview of the beam telescope used for track reconstruction is given.

Chapters 5 and 6 presents the measurements and results from the analysis and simulation respectively, followed by a comparison at the end of chapter 6.

Chapter 1

Semiconductor Detector devices

The equations in this chapter is primarily based on the books "Solid state physics: An introduction" by Philip Hofmann [2], "Introduction to solid state physics" by Charles Kittel [3], "Techniques for nuclear and particle physics experiments: a how-to approach" by William R. Leo [4], "Solid State Electronic Devices" by Ben G. Streetman and Sanjay K. Banerjee [5] and "The physics of semiconductors: With applications to optoelectronic devices" by Kevin F. Brennan [6].

1.1 Basic Concepts

The word *semiconductor* is a common term used to describe a subset of solid materials in the periodic table, or combinations of these, characterized by their conductive properties which lie between those of conductors and insulators. The conductivity in all solid materials can be understood from their band gap. Conductors and insulators have a very narrow and wide band gap, respectively, while semiconductor band gaps lie somewhere in between. The electrons can only cross the bandgap with sufficient energy, which further forms the basis for radiation detection with crystalline solids. The most widely used materials for radiation detection is silicon (Si) and germanium (Ge) as well as a few other compounds. New research is ongoing regarding the use of diamond as a semiconducting radiation detector. One important remark is that by adding impurities to the material, called doping, the conductivity can change by several orders of magnitude through adding "stepping stones" inside the bandgap.

Silicon has four valence electrons, which are electrons located in the outermost orbital of the atom. If one brings two or more Si atoms close together the valence electrons will be shared between the atoms, forming covalent bonds in a highly

ordered manner as shown in Figure 1.1. These electrons will be located somewhere between the two atoms in pairs. Since electrons are fermions and therefore obey the Pauli Exclusion principle[1], they have antiparallel spins and occupy two close-lying energy levels. Covalent bonds are highly directional, meaning that silicon atoms can form crystals in highly ordered structures called lattices [3].

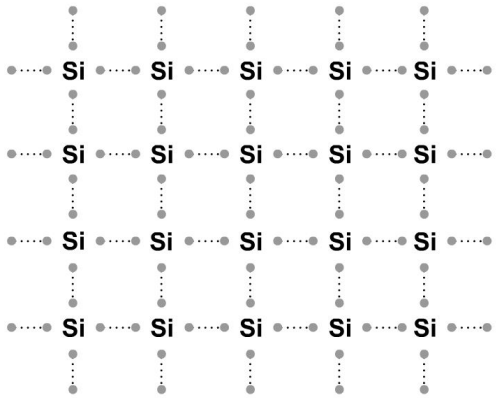

Figure 1.1: A silicon crystal lattice. The four valence electrons are shared with neighbouring atoms, forming covalent bonds [7].

1.2 Properties of Semiconductors

1.2.1 Bandgaps

As we know from quantum mechanics, electrons in an atom are confined to quantized energy levels. [5]. When two identical atoms are brought close together, their mutual interactions split the allowed energy states into two different levels. We can expand this to a more general case where we have N identical atoms with an inter-atomic distance d. Their interactions will then split the quantized energy levels into N new energy levels. If we now let N get very big and reduce the inter-atomic distance d to the atoms equilibrium distance, two semi-continuous bands will form. The bands consists of very densily spaced discrete energy states that the electrons can occupy . These two bands are called the conduction band and the valence band, respectively, see Figure 1.2. The region between the conduction and valence bands are called the *energy band gap*, which contains no available energy states for the electrons to occupy. The size of the bandgaps is what separates and defines insulators, conductors and semiconductors.

In semiconductors only the valence band energy states are filled at T = 0K and acts like an insulator. As the temperature increases, the electrons get an increasing probability of being thermally excited into the conduction band. When an electron

[1]The Pauli exclusion principle states that no more than two fermions (particles with half integer spin) can occupy the same energy state at the same time.

is excited from the valence band to the conduction band, it leaves a gap in the lattice of the material. This vacancy can be viewed as a positively charged quasi-particle called a *hole*. This hole is free to move in the band by diffusion. When an external electric field is applied across the semiconductor, the electrons start to move opposite to the direction of the field and can occupy the vacancy. This in turn opens a vacancy where the electron was before it started to move, and hence the hole moves with the direction of the field [5].

As stated before, a semiconductor is a material with conductive properties somewhere in between insulators and conductors, and their conductivity depends on factors such as carrier concentration, bandgap size and temperature.

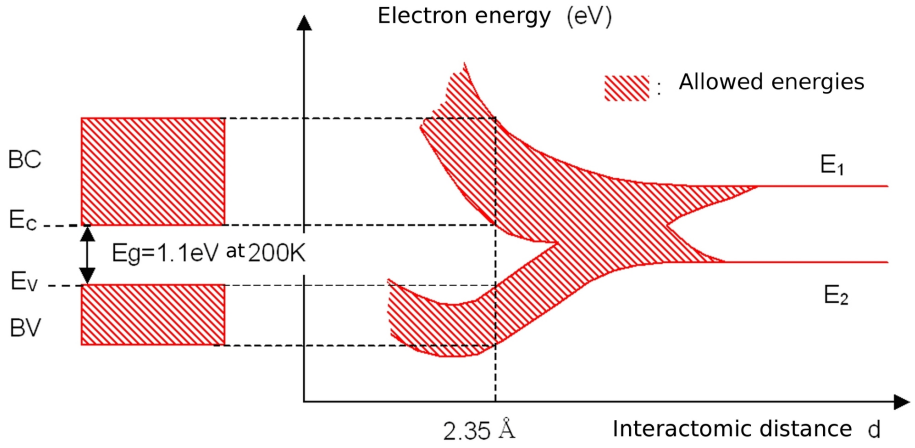

Figure 1.2: Here the splitting of energy levels into the valence- and conduction bands is shown. E_g is the energy gap, while E_v and E_c is the energy of the valence and conduction bands, respectively [8]

Since electrons obey the Pauli exclusion principle the electron distribution in the bands are governed by Fermi-Dirac statistics:

$$f(E,T) = \frac{1}{e^{\frac{(E-E_f)}{k_b T}} + 1} \tag{1.1}$$

- E is the energy of the electron
- E_f is the Fermi energy, sometimes called the chemical potential denoted μ
- k_b is the Boltzmann constant
- T is the temperature in Kelvin

The probability distribution of holes in the bands is simply $1 - f(E)$.

1.2.2 Doping

In an intrinsic (undoped) semiconductor, an electron would need at least an energy corresponding to the band gap in order to be excited into the conduction band. By adding a small amount of impurities to the silicon crystal, the conductivity can be significantly altered and the transition from valence to conduction band made easier.

By replacing a small amount of Si atoms with atoms that have five valence electrons, there would be an excess of electrons in the material. The atoms that contribute with an extra electron are called *Donors*. These excess electrons do not have any energy state to occupy in the already filled valence band and nor do they have the energy required to cross the bandgap. As a result, the excess electrons are loosely bound to the donor atom and occupy a state that lies slightly below the conduction band, inside the bandgap. This mechanism is known as n-type doping since electrons carry a negative charge, see Figure 1.3 a).

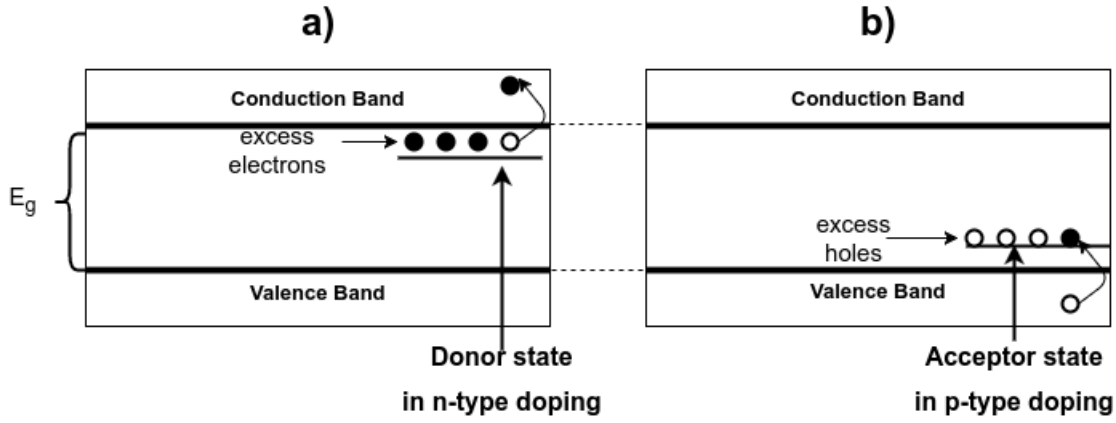

Figure 1.3: In a) we see the added energy level due to the donor atoms, and the excess electrons occupying it (filled circle). As illustrated, the electron is excited from this energy level into the conduction band quite easily, leaving a hole (empty circle) in the new energy level. In b) we see the added energy level due to the donor atoms, with excess holes occupying it and an electron being excited into that level and occupying the hole.

The reverse but similar case is the addition of atoms that lack one valence electron. These types of atoms are called *acceptors* because they will attract one of the neighbouring lattice electrons and bind them somewhat looser to the acceptor atom (since that has charge 3). This loose binding introduces an energy state that lies close to the valence band, inside the bandgap. This mechanism is known as p-type doping (Figure 1.3 b)).

The net result by doping is that the newly added energy levels inside the bandgap work like stepping stones for the electrons and holes that traverses it,

increasing the number of electrons that can reach the conduction band and contribute to current. The typical dopant concentration is 10^{18} dopant atoms per cm^3. Higher dopant concentrations are denoted by (+) and (++) to show how heavily doped the material is [9].

1.2.3 Majority and minority carriers

In a doped semiconductor there are two categories of charge carriers, majority and minority carriers. For an n-doped crystal the excess electrons from the donor atom fills the energy level just below the conduction band. From here it gets easily excited into the conduction band, thereby enhancing the conductivity. The electrons also fill up holes that form normally and therefore decrease the hole concentration, making the holes minority carriers and the electrons majority carriers.

In a p-doped crystal an analogous phenomena occurs. The holes from the acceptor atom fills up the energy level just above the valence band, making it easy for electrons to be excited into this new energy state. This leaves a majority of holes in the valence band that increases the conductivity, while the electrons acts as minority carriers.

1.2.4 Effects of doping

Electrons and holes may recombine in a pure semiconductor. This process becomes more frequent when impurities are added to the crystal. The doping introduces energy levels in the band gap that the electrons from the conduction band can fall into, called recombination centres. When the electron is located in one of these centres it can either annihilate with a hole or be released back into the conduction band after a certain holding time.

These centres reduce the time the charge carriers remains free. This should not be longer, or of the same magnitude, as the charge collection time. If the trapping time is longer than the collection time, charge will be lost and the detector will yield a weaker signal. Therefore, ultra-pure crystals are needed for semiconductor radiation detectors [4]

As we shall see, radiation damage can result in displacements of the crystal lattice and introduce more recombination centres and thus reduce the lifetime of the charge carriers.

1.2.5 Density of states and occupation probabilities

In the energy bands formed in semiconductors, the electrons have a range of energy states available for them to occupy and the distribution of energy states is given by the density of states for each band. A derivation of this can be found in [5]. In general this density of states can be expressed as

$$g(E)dE = \frac{1}{2\pi^2}\left(\frac{2m_e^*}{\hbar^2}\right)^{3/2} E^{1/2}dE, \tag{1.2}$$

where E is the electron energy, m_e is the electron mass, $\hbar$ is the reduced Planck constant. The units of the density of states is number of states per unit volume and energy in electron volts $[\#states/cm^3eV]$. It is proportional to the square root of the energy.

In the valence band and the conduction band, respectively, the density of states is altered. Since the band gap does not contain any energy states for the particles to occupy, the energy dependence in Eq. 1.2 must be changed. Therefore the energy of the states in the valence and conduction bands are given with respect to the bands edges E_V and E_C. The density of states in the valence band is given as:

$$g_V(E)dE = \frac{1}{2\pi^2}\left(\frac{2m_h^*}{\hbar^2}\right)^{\frac{3}{2}} (E_V - E)^{\frac{1}{2}}dE, E < E_V. \tag{1.3}$$

In the conduction band the density of states becomes:

$$g_C(E)dE = \frac{1}{2\pi^2}\left(\frac{2m_e^*}{\hbar^2}\right)^{\frac{3}{2}} (E - E_C)^{\frac{1}{2}}dE, E > E_C, \tag{1.4}$$

Where m_e^* and m_h^* is the effective mass of the electrons and holes respectively. This is a mass that is obtained from quantum mechanics and is inversely proportional to the curvature of the bands. E_C and E_V is the energy of the CBM and VBM respectively. All other variables are the same as in Eq. 1.2. The energy states in these bands are filled according to the Fermi-Dirac distribution function (Eq. 1.1) multiplied by g(E).

By integrating the Fermi-Dirac distribution function and the density of states over the available energies in the bands we can find the density of electrons (n) and holes (p) in the conduction and valence bands. To simplify the calculation, the Fermi-Dirac distribution can be simplified when the fermi level lies close to the

middle of the band gap:

$$f(E,T) \approx e^{-\frac{(E_F-E)}{k_B T}}, \tag{1.5}$$

for the electrons. For the holes this can be expressed as:

$$1 - f(E,T) \approx e^{\frac{(E-E_F)}{k_B T}}. \tag{1.6}$$

The density of electrons in the conduction band thus becomes:

$$n = \frac{1}{\sqrt{2}} \left(\frac{m_e^* k_B T}{\pi \hbar} \right)^{\frac{3}{2}} e^{-\frac{E_F - E_C}{k_B T}} = N_{eff}^C e^{-\frac{E_C - E_F}{k_B T}}, \tag{1.7}$$

and similarly for the holes in the valence band, we get:

$$p = \frac{1}{\sqrt{2}} \left(\frac{m_h^* k_B T}{\pi \hbar} \right)^{\frac{3}{2}} e^{\frac{E_V - E_F}{k_B T}} = N_{eff}^V e^{-\frac{E_F - E_V}{k_B T}}. \tag{1.8}$$

This is expressions of the carrier densities in both doped and pure semiconductors. With these carrier densities we can express the conductivity of them material σ. The conductivity of the material changes with the dopant concentrations according to

$$\sigma = e\left(n\mu_e + p\mu_h\right), \tag{1.9}$$

where n and p is the electron and hole concentrations, μ_e and μ_h are the mobilities of the charge carriers. From Eq. 1.9, we clearly see the impact of carrier concentrations on the conductivity, which is an important property of semiconductors.

The doping concentrations can be expressed in terms of resistivity ρ

$$\rho = \frac{1}{\mu e N}, \tag{1.10}$$

where N is the dopant concentration, e is the carrier charge, and μ is the carrier mobility. Resistivity is a property that can readily be measured in the sensor while the dopant concentrations itself cannot. Therefore this property is more useful when discussing doping levels.

1.3 The pn-junction

At room temperature, only a few electrons in silicon gain enough energy to be excited into the conduction band, and therefore they do not contribute significantly to the conduction. While holes also contribute to the conduction, the overall current is fluctuating and only contribute to detector noise. To change this, we can dope the silicon. If we were to put a n-doped crystal in close proximity to a p-doped crystal, we would get what is called a *pn-junction*. In a small region around the area where the two doped regions meet, electrons and holes start to diffuse. Electrons from the n-typed region recombine with holes in the p-type region leaving a vacancy (hole) in the n-doped region. This leads to both majority and minority carriers on both sides and to an opening of a region between the doped sides that is depleted of free charge carriers. In this region, a potential difference arises between the two sides, eventually stopping the electrons and holes from traversing it. This region is called the *depletion region*. The situation after the diffusion has stopped is shown in the top diagram of Figure 1.4.

In the p-doped region the chemical potential lies close to the valence band maximum (VBM), while in the n-doped region it is located near the conduction band minimum. In both cases the chemical potential is still located in the bandgap. This gives rise to another explanation of the pn-junction, stating that the chemical potential has to be constant through the whole system when the system is in thermal equilibrium [2]. To fulfill this, the energy bands bend, rising in the p-doped region and descending in the n-doped region. This is illustrated in Figure 1.4.

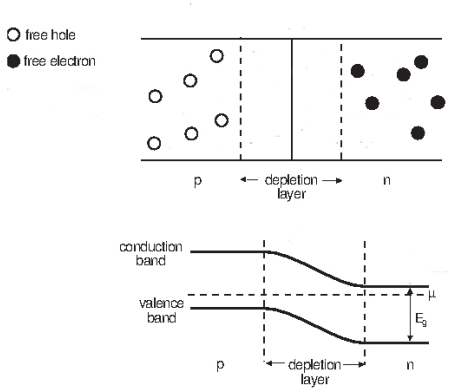

Figure 1.4: Top: The image shows the depletion region, together with the charge carriers, holes on the left side and electrons on the right side. Bottom: The bending of the bands is illustrated, where we can see that the chemical potential is constant throughout the volume, laying closer to the VBM on the p-side and closer to the CBM on the n-side. Modified from [10].

The equilibrium in the junction is not static, due to the minority carriers ability to get transported to the opposing side giving rise to a drift current. This drift current is compensated by a diffusion current stemming from majority carriers on either side moving into the opposing sides. These majority carriers, however, have to overcome the electrostatic force from the depletion layer and hence only electrons and holes with a sufficiently high energy contribute to the diffusion current.

1.3.1 Effects of externally applied voltages

The drift-diffusion dynamic can be substantially suppressed by an external applied voltage. This voltage, called bias voltage V_b, can be set up so that the cathode enters the p-doped side and the anode enters the n-type side setting up a *reversed bias*. With a reversed bias voltage the electrons and holes are drawn away from the junction, widening the depleted region until the entire volume is depleted of mobile charge carriers. In general the depletion width, w_d, is given by:

$$w_d = \sqrt{\frac{2\epsilon(V_b + V_i)}{N_d e}}, \tag{1.11}$$

where ϵ is the dielectric constant, V_i is the intrinsic potential across the junction, V_b is the applied bias voltage, e is the electron charge and N_d is the dopant concentration. In a detector of thickness, d, the entire depth are depleted at the depletion voltage

$$V_d = \frac{eN_d w_d^2}{2\epsilon} - V_i, \tag{1.12}$$

where N_d is the dopant concentration. The depleted volume now acts as a capacitor bounded by the p- and n-type semiconductor on each side, giving rise to a capacitance:

$$C = \epsilon \frac{A}{w_d} = A\sqrt{\frac{\epsilon e N_d}{2(V_b + V_i)}}, \tag{1.13}$$

where A is the materials surface area, ϵ is the dielectric constant of the material and N_d is the dopant concentration. A typical capacitance for a $100\mu m$ Si pn-junction is $1pF/mm^2$ [9].

Even though the junction is essentially free of mobile charge carriers in the depleted volume, thermally excited electrons can cross the bandgap and contribute

to a so-called *leakage current* that is dependent on the temperature.

1.3.2 Diode equation

A diode is a common general expression used to describe the pn-junction and different configurations of this. As it turns out, the current that flows through a diode can only flow in one direction due to the potential set up by the p- and n-doped regions. The current that flows through a diode is dependent on the bias voltage, whether it is reversed or forward, and is given by

$$I_{net} = I_0 \left(e^{+eV_b/kT} - 1 \right), \tag{1.14}$$

where I_0 is the leakage current in the absence of light and it is directly related to the recombination mechanism which implies that I_0 changes with the quality of the material and the temperature. V_b is the bias voltage, k is the Boltzmann constant and T is the temperature in Kelvin.

At the breakdown voltage, shown in Figure 1.5, the free electrons gets accelerated in the strong electric field and gain enough energy to break loose additional bound electrons, creating a large current gain in the diode.

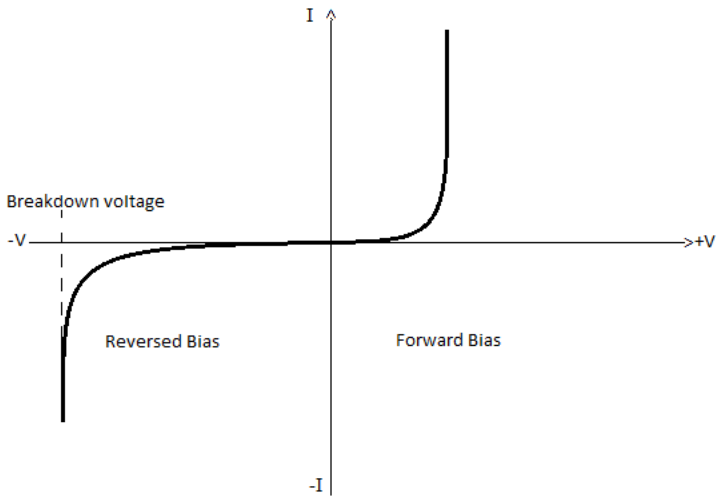

Figure 1.5: The current characteristics of a diode as a function of the bias voltage. On the right hand side we see how the current increases very rapidly with a forward bias narrowing the bandgap. On the left hand side the situation for a reversed bias is shown. Here the current is constant until a breakdown voltage is encountered with a sudden increase in current.

1.4 Pixel Sensors

Semiconductors works as radiation detectors much in the same way as an ionization chamber does. When a charged particle traverses the crystal it liberates electron-hole pairs in the crystal, but only the electrons and holes liberated in the depleted region start to drift and is collected on electrodes that are located on each side of the depleted region. The band gap in silicon pixel sensors is of the order of 1 eV so an energy of this order is enough to liberate one electron. In gaseous ionization chambers the energy required for liberating an electron is much higher (ca. 40 eV). The depletion region grows vertically with the detector thickness, and as such the depletion width equals the sensor thickness, see Figure 1.6. A planar pixel sensor is typically a thin silicon bulk with electrodes implanted on either side. The bulk and electrodes can be different configurations of doped silicon.

The electrodes is segmented into physically isolated pads in a planar matrix called pixels, and gives an unambiguous two-dimensional position resolution of particles that traverse the sensitive area. Furthermore, the pixels are surrounded by a guard ring that protects them from leakage currents. This guard ring is made up of several rings of electrodes where the voltage is reduced for each ring in order to terminate any field stemming from defects in the detector edges.

The last implementation is the readout electronics that the sensor are bump-bonded to. Bump-bonding is the process of attaching each pixel in the sensor to a pixellated readout circuit by metallic soldering bumps. Many different geometries and assemblies exists, and 3D pixel sensors are one of them.

1.4.1 3D pixel sensors

3D silicon detectors present a very radiation-hard sensor technology due to the electrodes short separation and the much smaller depletion regime. The electrodes are not implanted on the top and bottom of the silicon wafer as is the case for planar sensor, but cylindrical holes are drilled or etched into the bulk and filled with doped silicon. The depletion region is therefore completely decoupled from the thickness of the sensor thus giving more freedom in the design of readout electrodes, making it possible to implement very short inter-electrode distances. Shorter distances between electrodes and smaller depletion regions represent shorter drift times for the charge carriers and lower operational voltages. In a planar sensor the carriers could have to drift through the entire thickness of the detector, while in a 3D layout the maximum drift distance would be the inter-electrode distance [11]. Figure 1.7 shows a cross section through a 3D pixel detector.

The detector investigated in this thesis has a thickness of 230 μm with 336×80

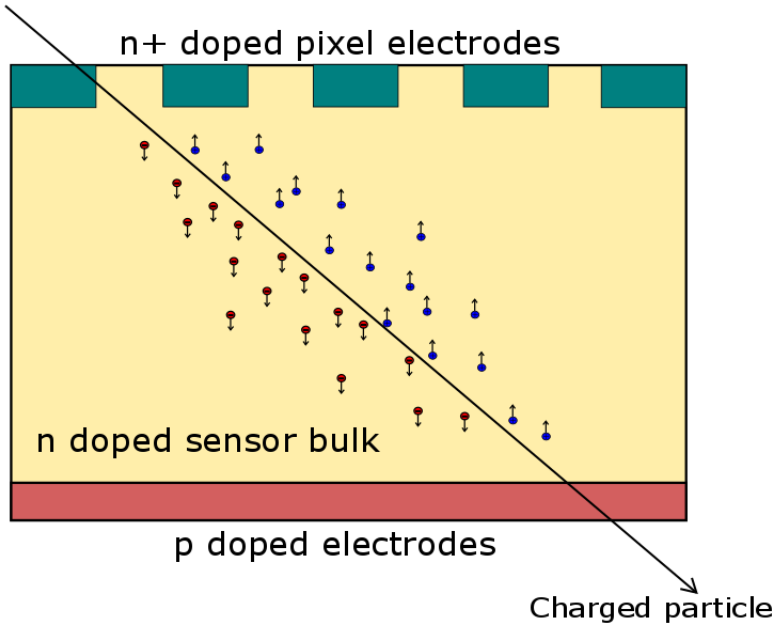

Figure 1.6: Cross section of a planar pixel sensor with n+ pixels implanted on the top of the n doped sensor bulk, and p doped readout electrodes on the bottom. Liberated electron-hole pairs are also shown as red (electrons) and blue (holes) dots drifting towards the respective electrodes. The electrons that are liberated closest to the n+ doped side will have the longest drift times, and the situation is similar for the holes liberated close to the p-doped side.

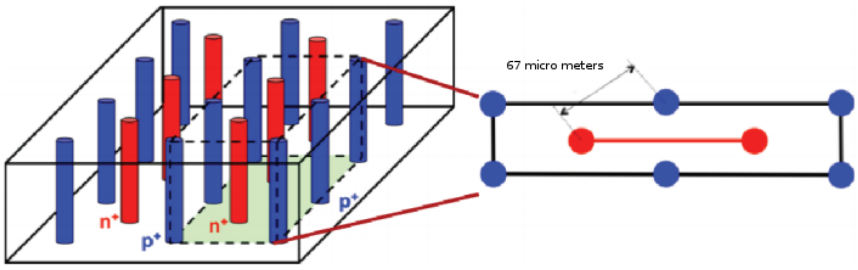

Figure 1.7: The figure shows the schematic layout of the 3D pixel detector. The dashed lines encapsulate a volume that corresponds to one pixel, and on the right hand side we can see the pixel cell as a top view. The red dots represents the readout electrodes while the blue dots are the ohmic electrodes that supplies the bias voltage. Modified from [12].

pixels that measure $50 \times 250\ \mu m^2$. As we can see from Figure 1.8, there are segmented squares that makes up the pixels with two shorted n^+ readout electrodes surrounded by 6 p^+ doped electrodes on the *BIAS grid* that encapsulates the pixels. The p-doped columns have a resistivity $\rho \approx 20 k\Omega cm$. These electrodes are bump bonded to a pixellated FE-I4b readout chip [13] that when supplied with a signal pulse

amplifies, shapes and measures the signal. The charge collection is explained more detailed in section 2.3.

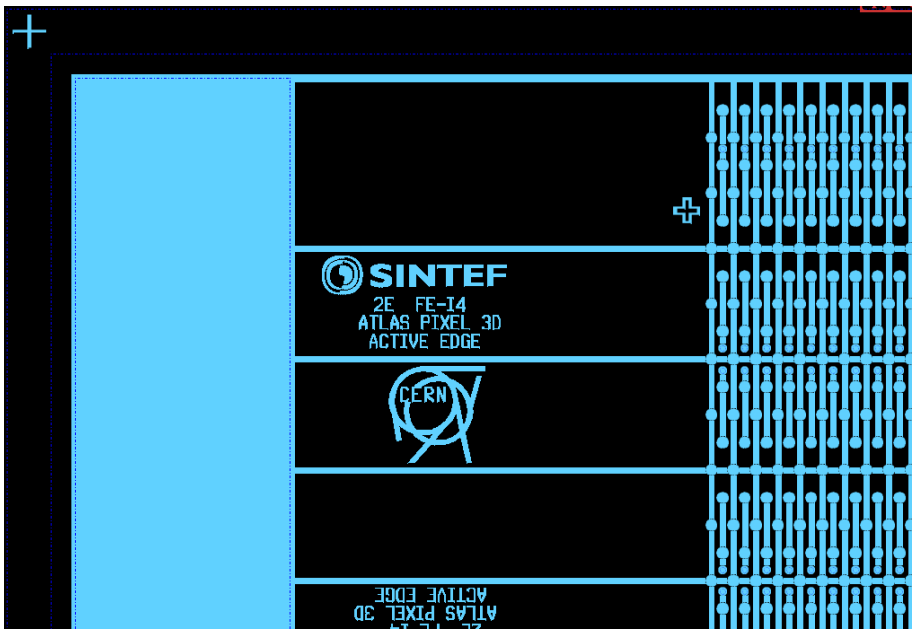

Figure 1.8: The image is of the electrode layout of a SINTEF 3D pixel sensor. The pixel sizes are $50 \times 250\mu m$ and the entire sensor contains 336×80 pixels. All the way to the left a large blue area can be seen, this area is the connection for supplying bias voltage. Note that the image are rotated 90 degrees, so the x- and y-directions is shifted and the shorter pixel width is in the y-direction. Towards the top we can see the edge pixels which are wider (containing 3 electrodes inside) than the normal ones, additionally the large area between the pixel grid and the bias pad is partially depleted and able to detect ionisation.

1.4.2 Active edge

One of the most useful properties of the 3D detector layout is that the edge is also capable of collecting charge. The planar sensor described in section 1.4 has a pixel matrix that is surrounded by guard rings in order to prevent leakage currents entering the sensitive area and thus increase the noise. The need for guard rings is eliminated in the 3D layout. When producing pixel detectors, the edge of the detector needs to be ended in some way i.e. by cutting the sensor. In a planar layout this cut needs to be done through the entire thickness of the crystal and therefore it can cause damage to the sensors electrodes. To prevent this from happening, the cut is done some distance from the electrodes and the gap is filled with guard rings to terminate the field and any leakage currents that are introduced with the damages.

For a 3D detector, a trench can be etched around the pixel matrix and then

doped. This enables depletion all the way to the edge and make this area active [14].

1.4.3 Radiation damage

Even though the potential difference of the p- and n-doped sides depletes the bulk of free charge carriers, a small fluctuating leakage current may still flow. This is due to thermally excited carriers and can introduce noise to the signal. Leakage currents can be increased by damage caused i.e. by the high radiation environment present in the LHC. Radiation damage cause lattice displacements, and severely impact the noise and collection times of the detector.

Lattice displacements are a product of interactions between the incident particle and the nuclei of the lattice atoms. To displace a silicon atom from its position in the lattice, a recoil energy of minimum 25 eV are required. When only such small energies are transferred to the Si atom, isolated displacements are created.

If the energy transfer in such an interaction is large enough, the particle can cause a cluster of displaced lattice atoms. While many of the displacements in such clusters fix themselves (called annealing process), some remain displaced. These clusters of displacements can be as large as tens of nanometers across. This has a much more severe impact on the detector performance because the displacements introduce more recombination centres inside the band gap, and hence increase the leakage current through the detector. Charge carriers may also be trapped in these defects for a certain time thus giving the alternate name trapping states or traps.

Carrier lifetimes are defined as the time it takes for i.e. an electron to recombine with a vacancy in the valence band via a trapping state. From the Shockley-Read-Hall recombination mechanism [15] [6] this is expressed as

$$\tau_i = \frac{1}{\sigma_i N_{trap} v_i}, \tag{1.15}$$

where N_{trap} is the number of empty traps in the material and v_i is the thermal velocity of the carriers. σ_i is the cross section for carrier capture and is a variable that defines the effective spatial cross section of the traps seen by the carriers trying to traverse it.

For heavily irradiated detectors the carrier lifetimes become shorter due to the increased number of trapping states in the material. By a comparison of the carrier lifetimes and the average collection times in the detector, we can understand that by reducing the distance between the electrodes (and hence the collection time) the radiation tolerance of the detector is increased.

Another type of damage caused by radiation is type inversion of the doped silicon. Removal of dopants by ionization of atomic electrons changes the effective doping concentrations. After a certain radiation dose, the n-doped silicon can start to behave like p-doped silicon.

To efficiently compare the damage caused by different types of particles with different energies, the term neutron equivalent fluence (n_{eq}) is used. This term is a measure of what damage the equivalent fluence of 1 MeV neutrons would cause to the material [16]. To reduce the effects of radiation damage one can decrease the collection time or decrease the drift distances, either by increasing the bias voltage or reducing the electrode separation. The latter is the case in 3D pixel detectors as it reduces the probability that a charge carrier will become trapped in one of the radiation induced defects.

Chapter 2

Energy Loss of Charged Particles and Signal Acquisition

Only electrons that have an energy greater than the bandgap-energy will contribute to current. While thermal excitations contribute with a small leakage current, electrons that are excited through interactions with charged particles will generate a much larger current through the junction. For particle tracking detectors, such as a pixel sensor device, the main interactions are those between heavy charged particles and the atoms, or their constituents, in the crystal lattice.

Equations in this chapter is primarily based on [4] [17] [2] and [9].

2.1 Energy Loss of Heavy Charged Particles

Generally two mechanisms dominate the energy loss of heavy charged particles (i.e charged pions) as they traverse matter:

1) Inelastic collisions with the atomic electrons.

2) Elastic scattering from the nuclei.

Other processes such as Cherenkov radiation, nuclear reactions and bremsstrahlung can also occur, but they are very rare in comparison with the first two. The inelastic collisions are by far the most observed interaction, and as they collide with the atmoic electrons, they transfer a fraction of their kinetic energy causing the atoms to be ionized or excited. The elastic scattering from the nuclei also occurs frequently

allthough the energy transfer in these interactions are very small. Therefore, the majority of the energy loss is due to the inelastic collisions. These occur with a quantum mechanical probability, but since the number of collisions per macroscopic path length is large, the statistical fluctuations in the energy loss are small and we can express the energy loss as an average over a unit path length. This quantity is called the stopping power, dE/dx, and is given by the *Bethe-Bloch equation* [4]:

$$-\frac{dE}{dx} = 2\pi N_a r_e^2 m_e c^2 \rho \frac{Z}{A}\frac{z^2}{\beta^2}\left[ln\left(\frac{2m_e\gamma^2 v^2 W_{max}}{I^2}\right) - 2\beta^2 - \delta - 2\frac{C}{Z}\right], \qquad (2.1)$$

the variables are given in Table 2.1.

Variable	Value / definition
r_e	The classical electron radius = $2.817fm$
m_e	the electron mass = $0.511MeV/c^2$
N_a	Avogadros number = $6.022 \times 10^{23}mol^{-1}$
I	mean excitation energy of the material (eV)
Z	the atomic number of the material
A	the atomic weight of the material
ρ	the density of the material
z	charge of the incident particle in units of e
β	= v/c of incident particle
γ	$= 1/\sqrt{1-\beta^2}$
W_{max}	maximum energy transfer in a single collision
δ	density correction
C	shell correction

Table 2.1: A list of all the variables in the Bethe-Bloch equation.

In figure 2.1 we can see how a muon with a range of energies loses energy as it traverses different materials. In the non-relativistic region, the particle energy loss is dominated by the $1/\beta^2$ factor, and the energy loss continues to decrease until a minimum at $v \approx 0.96c$ is reached. This minimum is more or less the same for all particles with identical charge, and particles in this energy region are called minimum ionizing particles (MIP). After the minimum, the curve rises again with the logarithmic term in Eq. 2.1, which is largely due to relativistic effects. Finally, for ultra-relativistic velocities, the particles energy loss reaches a plateau due to shell- and density corrections.

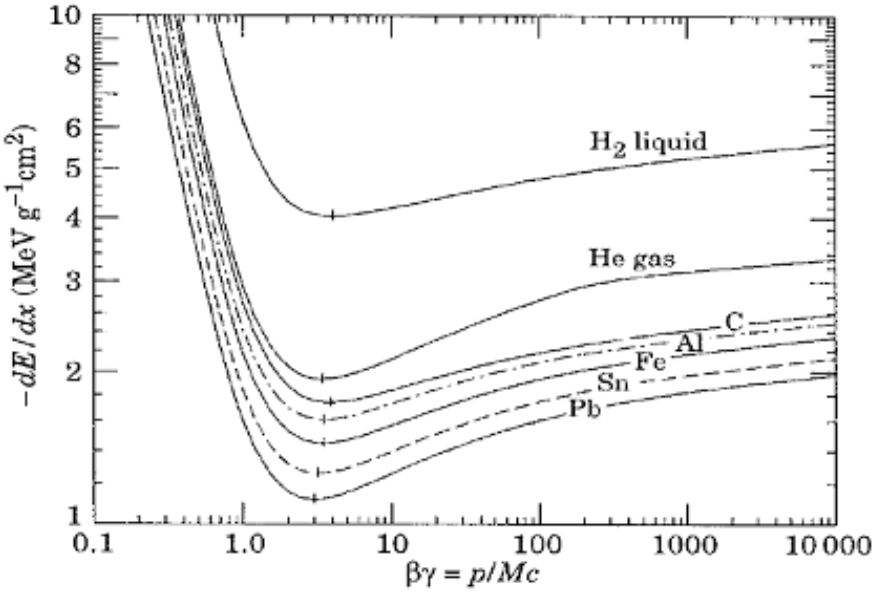

Figure 2.1: Muon energy loss per unit length as a function of $\beta\gamma$. The lines represent a particles energy loss in different materials. At $\beta\gamma = 3$ we observe that the muon acts as a minimum ionizing particle in all the materials. Figure retrieved from [18].

2.1.1 Energy straggling and the Landau distribution

Charged particles that pass through a thickness of matter will have a mean energy loss described by the Bethe-Bloch equation (Eq. 2.1). Theoretically, the energy loss distribution is divided into two categories; thick and thin absorbers. In our case we are only interested in the thin absorber case as the sensor thickness for pixel devices are only a few hundred micrometers.

The energy loss distribution in thin absorbers is a complicated calculation due to the probability of high energy transfers in a single collision, where W_{max} is the upper limit for heavy charged particles. For electrons, Bremsstrahlung can account for up to one half of their energy loss, giving rise to the long tail seen in Figure 2.2. Landau, Symon and Vavilov have carried out theoretical calculations for different regions of applicability. The important and common parameter in these calculations is the ratio

$$\kappa = \overline{\Delta}/W_{max}, \tag{2.2}$$

where $\overline{\Delta}$ is the mean energy loss, and W_{max} is the maximum energy transferred in a single collision.

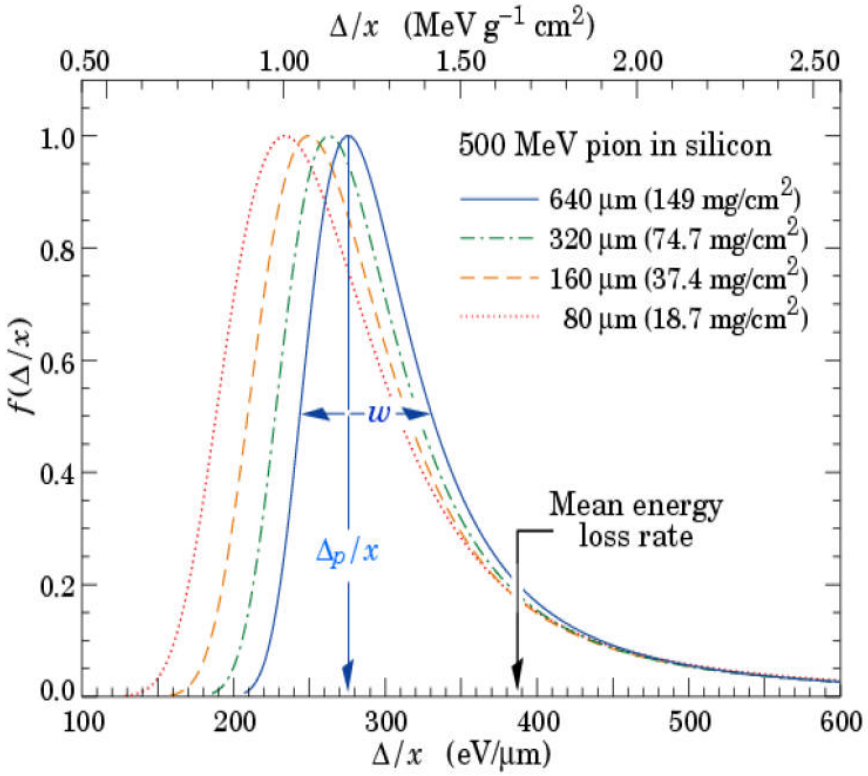

Figure 2.2: The Landau distribution for a 500MeV Pion in layers of silicone with different thickness. The curves are normalized to unity at the most probable value $\Delta p/x$. w is the full width at half maximum [19].

The mean energy loss can be calculated by Eq. 2.1 but is usually approximated by ignoring the logarithmic term yielding

$$\overline{\Delta} \simeq \xi = 2\pi N_a r_e^2 m_e c^2 \rho \frac{Z}{A} \left(\frac{z}{\beta}\right)^2 x. \tag{2.3}$$

Landau's theory applies to the cases where $\kappa \leq 0.01$ where three assumptions are made:

1) the maximum energy transfer permitted is infinite. $W_{max} \to \infty$.

2) the individual energy transfers are sufficiently large such that the electrons may be treated as free. (energy transfers from distant collisions is ignored)

3) the particle maintains a constant velocity through the material.

The distribution is expressed as

$$f(x, \Delta) = \Phi(\lambda)/\xi, \tag{2.4}$$

where $\Phi(\lambda)$ is a universal function dependent only on λ and is given as

$$\Phi(\lambda) = \frac{1}{\pi} \int_0^\infty e^{(-u \ln u - u\lambda)} \sin \pi u du, \tag{2.5}$$

with

$$\lambda = \frac{1}{\xi} \left[\Delta - \xi(\ln \xi - \ln \epsilon + 1 - C)\right], \tag{2.6}$$

where C = 0.577 is the Euler constant and

$$\ln \epsilon = \ln \frac{(1 - \beta^2)\, I^2}{2mc^2\beta^2} + \beta^2. \tag{2.7}$$

Here ϵ represents the minimum energy transfer according to assumption 2). $\phi(\lambda)$ is a function dependent only on λ and can only be solved numerically. From an evaluation of $\phi(\lambda)$ the most probable energy loss is found to be

$$\Delta_{mp} = \xi \left[\ln(\xi/\epsilon) + 0.198 - \delta\right]. \tag{2.8}$$

2.2 Multiple scattering

When a charged particle traverses the detector it is deflected by many small-angle scatterers, mainly due to Coulomb interactions with lattice nuclei. For hadrons the strong interaction also contributes to this deflection. The scattering angle of the particle after leaving the detector thickness and many small-angle scatterings follows a Gaussian distribution with an root mean square (rms) of

$$\theta_{plane}^{rms} = \frac{13.6MeV}{\beta pc} z \sqrt{\frac{x}{X_0}} \left[1 + 0.038 \ln\left(\frac{x}{X_0}\right)\right], \tag{2.9}$$

where X_0 is the radiation length, which is a material dependent measure of the energy loss of a particle due to interactions over a distance in that material. p is the particle momentum in MeV, β is the velocity of the particle in units of the speed of light, z is the charge of the incident particle and x/X_0 is the thickness of the traversed material in units of the radiation length. In silicon the radiation length is 9.36 cm, and a pixel detector in the LHC has a thickness of 2% of the radiation length giving a trajectory change for a 1 GeV particle of approximately 0.1 degrees [20].

2.3 Signal Acquisition

2.3.1 Charge collection

Semiconductors need a very small average energy deposition in order to create an electron-hole pair. A charged particle passing through a sensor bulk will in general liberate one order of magnitude more carriers than in a gaseous ionization detector. In silicon the mean energy for electron-hole production is 3.62 eV at room temperature. The band gap in silicon is on the order of 1 eV wide, so less than a third of the energy is actually spent on liberating charge carriers. The remaining two thirds go into exciting lattice vibrations (phonons).

Electrons and holes move in opposite directions but contribute equally to the signal current, with the same polarity due to their opposite charge. The time it takes for a carrier to traverse the bulk is called the collection time. The transport of electron/hole pairs in the presence of an electric field is called drift. The characteristic time for phonon excitations is much smaller than the collection time, so the carriers are always in equilibrium with the lattice. Carriers in equilibrium with the lattice have a velocity only dependent on the electric field E, and is given by

$$\vec{v} = \mu\vec{E}, \tag{2.10}$$

where μ is the mobility of the carrier which is linked to the diffusion constant D, through the Einstein relation

$$\mu = \frac{e}{kT}D. \tag{2.11}$$

Thermal energy causes carriers to move in random directions, but colliding more in one direction giving rise to a concentration gradient. The net motion of

the carriers is therefore in the opposite direction of the concentration gradient. The diffusion spreads out with time as

$$\sigma = \sqrt{Dt}. \tag{2.12}$$

Assuming full depletion, the time required for a charge to traverse the depleted region and be collected at an electrode (collection time) is given in [9] as

$$t_c = \frac{d^2}{\mu V}, \tag{2.13}$$

where d is the depth the charge carrier will need to traverse, μ is the mobility and V is the bias voltage.

When radiation with energy E hit material with mean energy, w, required for electron-hole production, E/w electron-hole pairs are created. For silicon $w = 3.36$ eV. Furthermore, assume a collection efficiency, ϵ, so that a charge $Q = \epsilon E/w$ is collected at the electrodes, then the observed voltage on the electrodes is

$$V = \frac{Q}{C} = \epsilon \frac{E}{wC}, \tag{2.14}$$

where C is the capacitance given in Eq. 1.13.

The most probable energy loss of traversing particles in thin layers of materials is given by Eq. 2.8.

2.3.2 The Shockley-Ramo theorem

Although the term "charge-collection" is used when describing how the liberated charge carriers produce a signal in the detector, it is not describing the actual process of how a charge creates a signal on the electrodes. William Shockley and Simon Ramo independently derived a theory of how moving charges induces a current on an electrode in their vicinity, named the Shockley-Ramo theorem [21]. The general expression for an induced current on an electrode in the vicinity of a moving charge carrier is found in [9], and it is

$$i_A = e\vec{v}\vec{E}_v, \tag{2.15}$$

where e is the electron charge, $\vec{v}$ is the velocity of the charge carrier and $\vec{E}_v$ is the weighting field [22]. The weighting field is not the same as the electric field, and depends on the electrode geometry. This weighting field determines how the charge couples to an electrode and how it induces a current on it.

2.3.3 Time over threshold

When the charge is collected at the electrodes a voltage pulse is received in the readout chip. This pulse is amplified and shaped before its time over threshold (ToT) is measured.

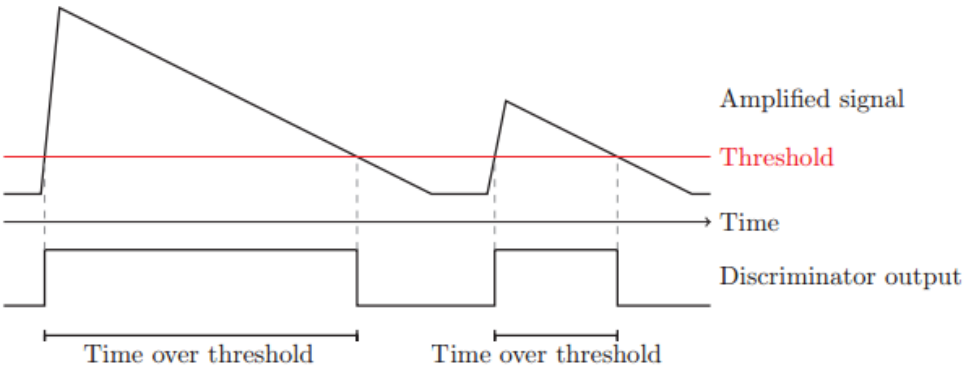

Figure 2.3: The figure shows how the signal pulse is rising above a threshold before it falls down slowly as the capacitor are discharging. The time the signal stays above the threshold are measured as illustrated by the bottom line [14].

The ToT is a measure of how long a given signal pulse stays above a digitally set threshold. Which is given in units of the LHC's bunch crossing time (25 ns), meaning that a measured ToT of 8 implies that the signal stayed above threshold for 8×25 ns $= 200$ ns.

The ToT is dependent on the radiation energy, as the number of liberated charge carriers that are collected are proportional to the energy deposition. The collected signal charges up a capacitor in the readout electronics and is discharged. The charging is usually relatively fast while the discharge goes slower, this is illustrated in Figure 2.3.

2.3.4 Detector efficiency

The efficiency of the pixel detector is perhaps the most important parameter to be determined before it is put into use, and is indeed one of the key features investigated

in this analysis. Efficiencies in pixel detectors are divided into two categories; *absolute* and *intrinsic* efficiencies. The absolute efficiency is a product of the intrinsic efficiency and the geometrical acceptance

$$\epsilon_{absolute} = \epsilon_{instrinsic}\epsilon_{geometric}. \tag{2.16}$$

We would, however, like to find the intrinsic efficiency which is the fraction of particles that are counted as events in the detector out of all particles passing through the it. Since the number of particles in the beam is unknown we cannot say anything about the absolute efficiency but by using a reference detector to count the particles passing through our detector we can find the intrinsic efficiency as

$$\epsilon_{instrinsic} = \frac{N_{registered}}{N_{incoming}}. \tag{2.17}$$

In semiconductor detectors the intrinsic efficiency is generally excellent for charged particles, while neutral particles are much harder to record. Detection of neutral particles rely upon their secondary charged particles, and those interactions are rare in thin layers of silicon [4].

The uncertainty in the detector efficiency can be calculated by finding the standard deviation of the counted number of hits in the DUT. This is done by assuming that the intrinsic efficiency found by Eq. 2.16 is a binomially distributed variable, where one finds the count of "successes" $N_{registered} = n$ out of $N_{incoming} = N$ independent trials, and where the variance is given as

$$\sigma_n = \sqrt{NPq} = \sqrt{N\epsilon(1-\epsilon)}, \tag{2.18}$$

where $\epsilon = \frac{n}{N}$ is the efficiency. Furthermore, the standard deviation is given as the square-root of the variance, so the standard deviation of the efficiency becomes

$$\sigma_\epsilon = \frac{\sigma_n}{N} = \frac{\sqrt{n(1-\epsilon)}}{N}, \tag{2.19}$$

which is the uncertainty used in the efficiency calculations in chapter 5 [23].

Chapter 3

The Large Hadron Collider and the ATLAS Experiment

The European Organization for Nuclear Research (CERN) is a research collaboration located on the French-Swiss border. Here physicists and engineers from 22 member states collaborate to unravel the mysteries of the universe that surrounds us. Approximately 100 metres beneath the ground sits the LHC, with its 4 largest experiments; ATLAS, ALICE, CMS and LHCb.

Since 2009, the LHC have delivered high energy particle collisions to the four large experiments along its circumference. All are built to study the fundamental building blocks of matter and their interactions, commonly known as the standard model of particle physics. Since 2012 these four experiments have been assigned to search for new exotic particles and subatomic phenomena. This search requires much higher collision energies, and a higher collision rate or *luminosity* which imposes strict requirements on the radiation hardness and lifetimes of the detector components [24].

3.1 The Large Hadron Collider

The LHC is in fact the last step in a chain of accelerators who each boosts the particles' energies by an increasing amount, up to near the speed of light, see Figure 3.1.

In order to obtain single protons for usage in proton beams, the electrons are stripped from hydrogen atoms in an electric field. Furthermore, the protons need to gain a certain amount of energy before they are injected into the LHC. This is done

through several accelerating steps starting with the Linear Accelerator (LINAC). Here the protons are accelerated up to approximately 50MeV before they are injected into the Proton Synchrotron Booster (PSB). From the PSB, protons are injected into the Proton Synchrotron, and finally into the Super Proton Synchrotron. In the SPS the protons gain energies up to 450GeV before they are injected into the LHC in two opposite directions. In Figure 3.1 all the abovementioned accelerators are shown, in addition to a few others. Once in the LHC, the protons are circulating clockwise and counter-clockwise in two separate beamlines before they are brought to collide in one of the four experiments [25].

The beam in the LHC are divided into bunches, where each bunch consists of a very large number of protons, each with an average energy of 6.5 TeV. The bunches revolves around the 27 km long accelerator with a spacing of 25 nanoseconds. This means that there occurs a collision at each experiment every 25 ns.

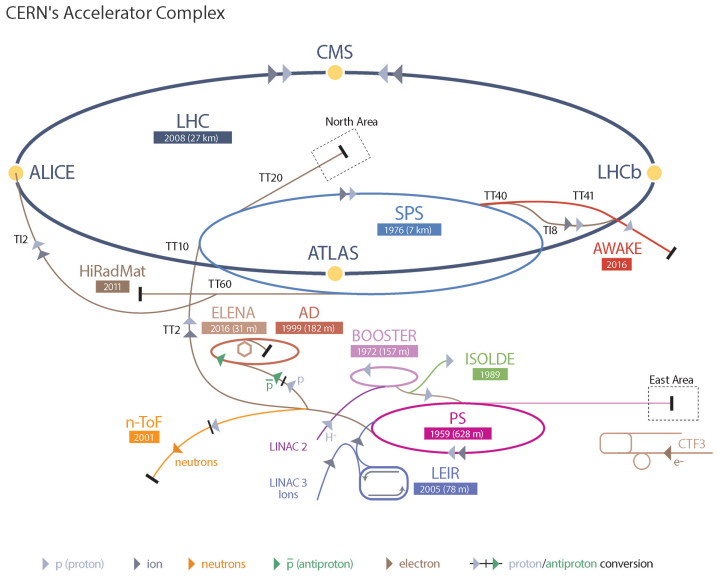

Figure 3.1: An overview of the accelerator complex at CERN. Located on the LHC (largest ring) the four experiments; ATLAS, ALICE, CMS and LHCb can be seen. Retrieved from [26]

In order to fully understand the discussion about the LHC, its composite parts and the impact this has on high energy physics (HEP) experiments, we need to introduce a few concepts, such as luminosity and cross section.

3.1.1 Luminosity

In a high energy physics experiment, designed to create and observe new phenomena and particles, the luminosity is an important parameter. This is the quantity that measures the accelerators ability to produce a required number of events, and are the proportionality constant between the number of events per second dN/dt and the cross section σ_p

$$\frac{dN}{dt} = \mathcal{L}\sigma_p, \tag{3.1}$$

where $\mathcal{L}$ is the luminosity.

For a colliding beam experiment the bunches of the beam traverse each other and therefore not all particles collide. While it can be hard to analytically calculate the distribution of particles inside a bunch, it is often justified to assume that they follow a Gaussian distribution in all directions, i.e. the core of the distribution contribute to the collision rate and thus the luminosity. Furthermore, there are N_1 particles in one of the bunches and N_2 in the other, with a revolution frequency f. Given the number of bunches N_b we end up with an expression for the luminosity:

$$\mathcal{L} = \frac{N_1 N_2 f N_b}{4\pi\sigma_x\sigma_y}[cm^{-2}s^{-1}], \tag{3.2}$$

where σ_x and σ_y denotes the bunch dimensions that are Gaussian distributed. One can also include many correction factors to these formulas that are a product of how the beams are shaped when entering the different experiments [27].

3.1.2 Center of mass energy

We can describe the center of mass energy in two different contexts. That of a colliding beam experiment, where the particles of two beams are colliding, and that of a fixed target experiment. The center of mass energy describes the energy available for particle production and this energy is dependent on the momentum of the primary particles that are colliding.

The kinematics of a particle with mass m, can be expressed in terms of its momentum $\vec{p}$ and energy E as a four-vector $P(E, \vec{p})$;

$$P^2 = E^2 - \vec{p}^2 = m^2. \tag{3.3}$$

When two beams are colliding, or rather two particles, the total centre of mass energy can be expressed as

$$(P_1 + P_2)^2 = E_{cm}^2 = (E_1 + E_2)^2, \tag{3.4}$$

where the momentum term vanishes when the collision point is at rest in the laboratory frame, ($\vec{p_1} = -\vec{p_2}$).

For a fixed target collision only one of the particles have momentum (i.e $\vec{p_2} = 0$) so the expression becomes

$$E_{cm}^2 = (m_1^2 + m_2^2 + 2m_2E_1). \tag{3.5}$$

3.1.3 Cross section

Cross section describes the probability of a collision between two beams and what particles it will generate. The ATLAS experiment is looking for new physics, i.e. new exotic particles and hints of Super Symmetry (SUSY). The cross sections for such phenomena are very low, and thus a very high luminosity are required, as can be seen from Equation 3.1 .

Cross section has the unit of area ($barn^2$ $[b^2] = 1 \times 10^{-28} m^2$) since it describes the form and probability of an interaction between particles. However, the area in the cross section should not be mistaken with a geometrical interpretation of the particles [28].

3.2 The ATLAS Experiment

Of the experiments at CERN that utilizes the beam from LHC, the ATLAS detector is the largest. It searches for new phenomena, and as such are built as a general purpose detector that records every event (produced particle) in a collision. The detector are built in several layers in a barrel configuration around the collision point, with a length of 46 m and a diameter of 25 m.

To detect every particle that are created in a collision, the ATLAS detector are built up of four subsystems, 1) the inner detector (ID) 2) the calorimeters 3) the muon system 4) the magnet systems. Figure 3.2 shows an overview of the ATLAS detector.

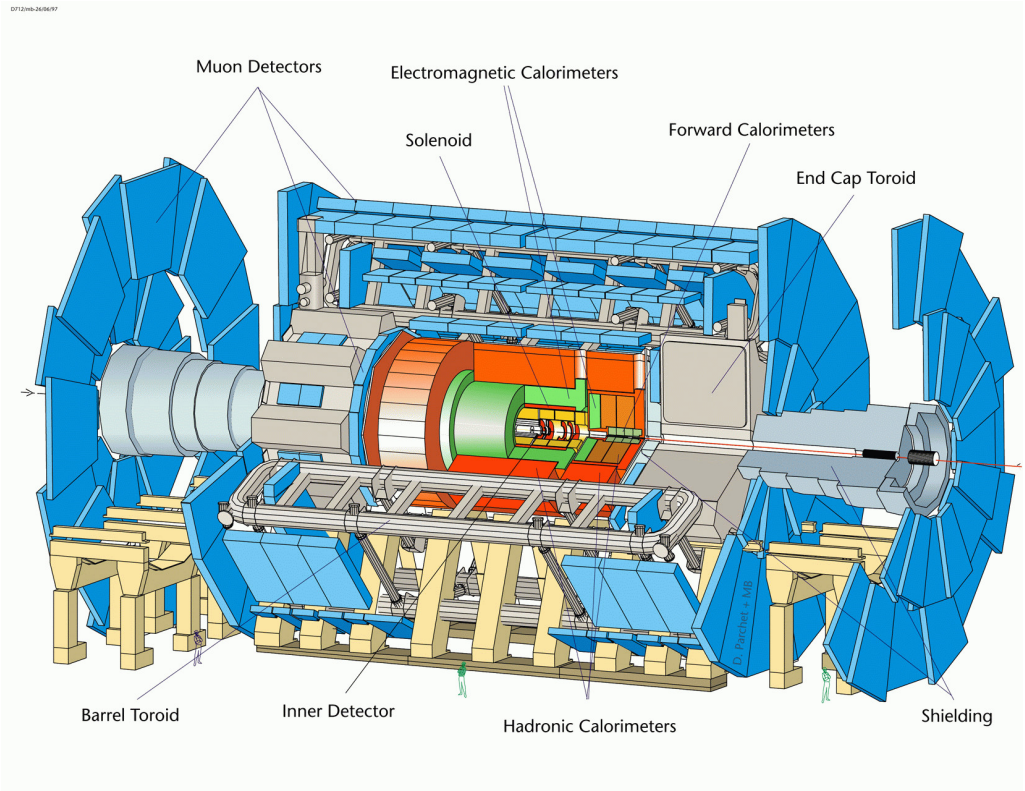

Figure 3.2: Overview of the ATLAS detector [29].

1) The inner detector combines high resolution detectors closest to the beam line and coarser tracking detectors further out, with the purpose of measuring the particles momentum and the vertices of decaying particles. In order to resolve vertices and momentum measurements close to the beam line, high resolution tracking detectors are needed. The density of tracks (occupancy) falls off with distance from the collision point, meaning that coarser resolution detectors can be used there. This is realized by having several layers of semi-conductor pixel sensors close to the beam line and silicon tracking detectors (SCT) and transition radiation trackers (TRT) further out.

As layers are added outward from the beam line, the area that needs to be covered increases. The cost of pixel detectors is much higher than for SCTs or TRTs and therefore the latter ones are used further out as more coarsly segmented detectors are acceptable there [30].

2) The calorimeters of the ATLAS detector have the purpose of stopping the particles and measure their energies. The calorimeter system consists of the electromagnetic calorimeter (ECAL) and the hadronic calorimeter (HCAL). The ECAL makes up the next layer of subsystems after the TRT. Here the energy of electromagnetically interacting particles is measured, but not all are stopped here. Some protons may

continue into the HCAL, while muons, which are MIPs, can fly through the entire detector without stopping. particles that are not fully stopped in the ECAL continue into the HCAL. The HCAL have the purpose of measuring energies of neutral particles and to fully stop the hadronic decayed particles such as protons and neutrons. In Figure 3.2 the location of the ECAL and HCAL are shown.

3) The muon system consists of a large area of ionization chambers. Since all other particles produced are stopped before they reach the muon system, the detectors here only need to be able to detect ionisation.

4) The last sub system in the ATLAS detector are the magnets. A solenoid magnet with a strength of $\approx 2T$, are located just outside the inner detector and serves the purpose of bending the particle trajectories so that momentum may be measured. The second magnet system are located between the HCAL and the muon chambers also bending the tracks of the particles.

An important parameter not discussed is the missing transverse energy. This is due to neutrinos that leave no track in any of the detector systems. By reconstructing the energy and momentum of all the other particles created in a collision, the missing transverse energy carried away by the neutrino is found in addition to its most probable direction.

Figure 3.3 shows how different particles are detected in the subsystems of ATLAS, and where they are stopped.

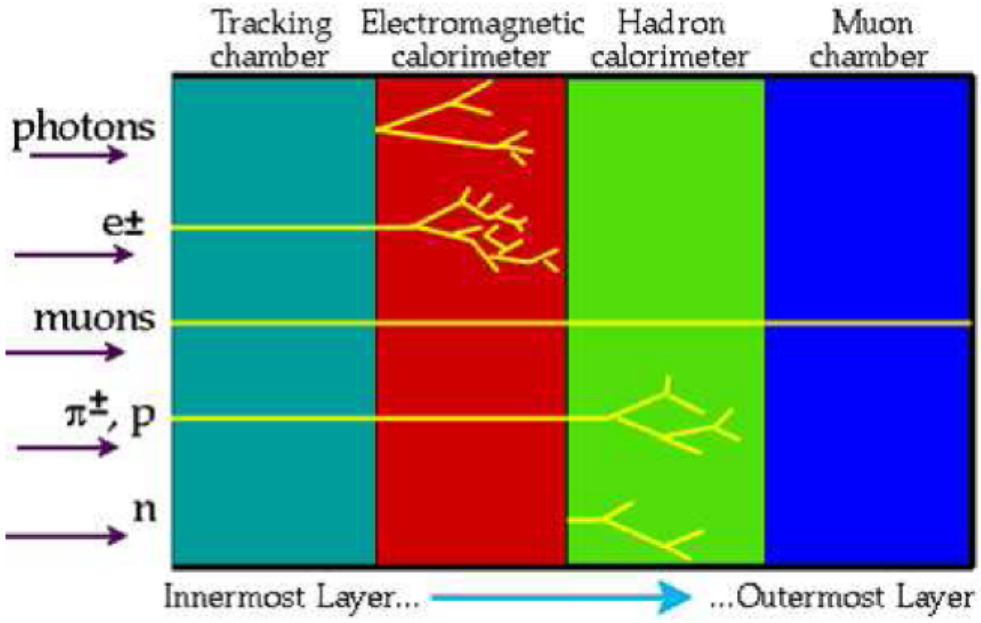

Figure 3.3: Different particles are stopped in the different layers in the ATLAS detector [30].

With collisions happening every 25 ns, there is a need to reject certain events in the data. This is done either by triggers in the individual subsystems, recording only certain specified events and rejecting others. Further data suppression are done offline.

3.2.1 The ATLAS inner tracker upgrade

The number of events per collision is expected to increase from 25 up to 140-200 per collision when the LHC is upgraded. This will give a large increase in occupancy and radiation levels in the experiments, and the entire ATLAS inner detector will be upgraded to withstand this.

The current inner detector will be replaced by an all silicon tracking system with the 5 innermost layers being pixel detectors and 4 outer layers of silicon strip detectors, named the ITk. The 3D pixel detector prototype analysed in this thesis are one of the proposed technologies that are under consideration for use in the innermost layers of the ITk.

The general layout of the inner tracker is not yet decided and studies are ongoing to figure out the best configuration [31].

Chapter 4

Description of the Testbeam Facility and Setup

Facilities that can deliver high energy particle beams for testing purposes are a crucial link between concept and implementation of new detector technologies. These testbeams play a dominant role in calibration and development of new prototypes and give a good introduction for students new to the field. At CERN two such testbeam facilities exists, the north area and the east area. The north area is supplied by the 450 GeV proton beam from the SPS. The beam is delivered onto targets from which four secondary beams are steered to testbeam user areas [32].

The secondary beam used in this analysis is a pion beam of 120 GeV. This beam originates from the proton beam colliding into a beryllium target, and further focused through a series of collimators and magnets before it is delivered through beam line H6 (see Figure 4.1).

4.1 Testbeam Setup

The users area at the testbeam site includes a pixel sensor *beam telescope*. This telescope consists of six planes of highly calibrated monolithic pixel sensors, providing a reference of the particle tracks for the sensors we are testing, known as devices under test (DUT). There is a very well-calibrated mechanical mounting structure for mounting the DUTs. In addition it also has a readout system that is flexible and easy to use (EUDAQ) and four scintillators that are connected to photomultiplier tubes and operated in coincidence for trigger purposes[1]. All these components are

[1] A trigger is a signal that is externally supplied to the DUTs in order to provide a time stamp to when and where a particle is passing through the telescope. Operation in coincidence means

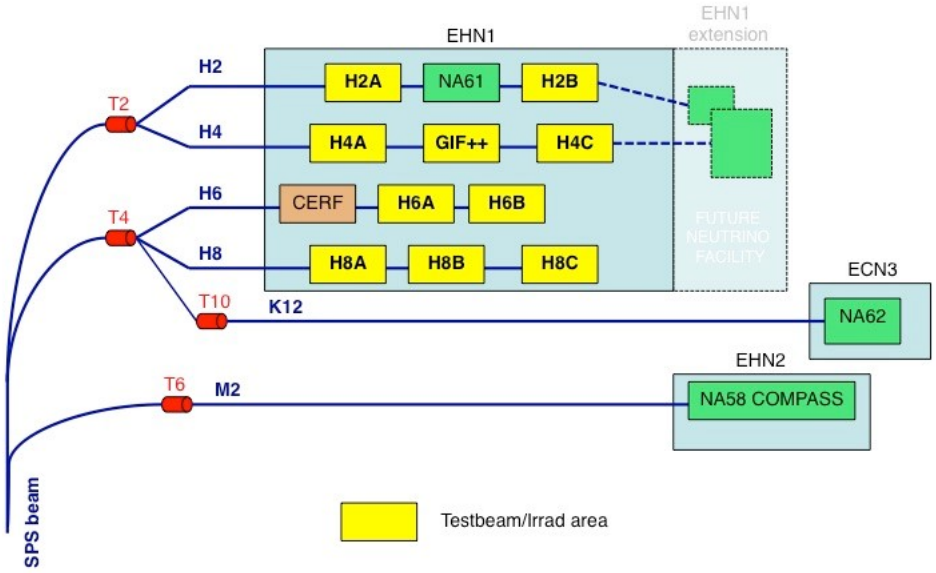

Figure 4.1: Schematic of the north area at CERN, H6A and H6B were the areas we used for the testbeams [33].

optimized for measurements of the DUTs.

In a user area, several groups from different Universities tests their DUTs simultaneously. This imposes a challenge with regards to when one run (extended period of data collection) should be ended and new one started. Obviously, some degree of cooperation is necessary, and the groups take alternating shifts in the provided control room. Here the users can get online feedback in order to check that the DUTs is fully functioning by observing histograms of the detector response that fills up continuously during the data taking. The users also controls the bias voltages supplied to the DUTs and monitor the leakage currents.

In order to collect as much good data as possible, the groups provide the people on shift with configuration files for their DUTs. These files contain the tuning of the DUTs, determining what response the DUTs should have for a certain number of released charge carriers. Additionally, the users monitor their DUTs online in a separated control room.

that both the front and back side scintillators needs to receive a signal.

4.1.1 The EUDET beam telescope

The beam telescope used in the north area is a so-called EUDET-type beam telescope. These types of telescopes have six planes of ultra thin ($\approx$ 50 μm thick) Mimosa-26 monolithic pixel sensors with a fast and very precise readout. A monolithic pixel sensor is a sensor that have the readout on-chip and thus no external readout chips are needed.

The Mimosa-26 sensor consists of approximately 660 000 pixels, 1152 columns and 576 rows with a pixel pitch of 18.4μm. The rows are read out one by one in a rolling shutter mode while the columns can be read out in parallel. This enables the Mimosa sensor to read out the entire pixel matrix in 112μs (or $\approx$ 10k frames a second), while simultaneously read out multiple hits. This imposed certain problems in the analysis as previous events may still be contained in the buffer of the Mimosa sensor while the DUTs register a new event. This was resolved by imposing a strict requirement on the accepted tracks passing through the DUTs, and is further explained in Section 5.2.2. The efficiency of the Mimosa-26 sensors has been measured to be $99.5 \pm 0.1\%$ with a spatial resolution that has been found to be $2.1 \pm 0.4 \mu m$ [34].

The Mimosa sensors are mounted in a configuration as shown in Figure 4.3. With planes 0-2 and 3-5 referred to as upstream and downstream, respectively. The DUTs mounting space is located between plane 2 and 3, the mounting structure for the DUTs is highly modular and allows for tilted sensor setups just as easily as normal incidence angles. The SINTEF sensors were set up as shown in Figure 4.2 for the 2015 and 2016 testbeams.

Additionally, the DUTs can be placed inside a cooling box that can cool the sensor down to $\approx -30°C$. This cooling is necessary in order to operate irradiated sensors without too high leakage currents that affects the signal. Since radiation damage introduces lattice displacements and thus more recombination centres, the leakage current increases dramatically due to thermal excitations. This problem is reduced by cooling down the sensors inside this cooling box.

The parameter $\epsilon = \Sigma_i x_i / X_{0,i}$ defines the *material budget* which describes the total thickness of the materials located in front of the beam normalized to the materials radiation lengths (X_0). From Eq. 2.9, it is apparent that this parameter gives the expected scattering angle from multiple scattering throughout the length of the telescope.

Scintillation detectors are located in front of plane 0 and behind plane 5. Each detector consists of two crossed scintillator planes connected to PhotoMultiplier Tube (PMT) detectors. Together, these four scintillating planes cover an area of 20×10 mm that defines the spatial acceptance for the triggers in the telescope.

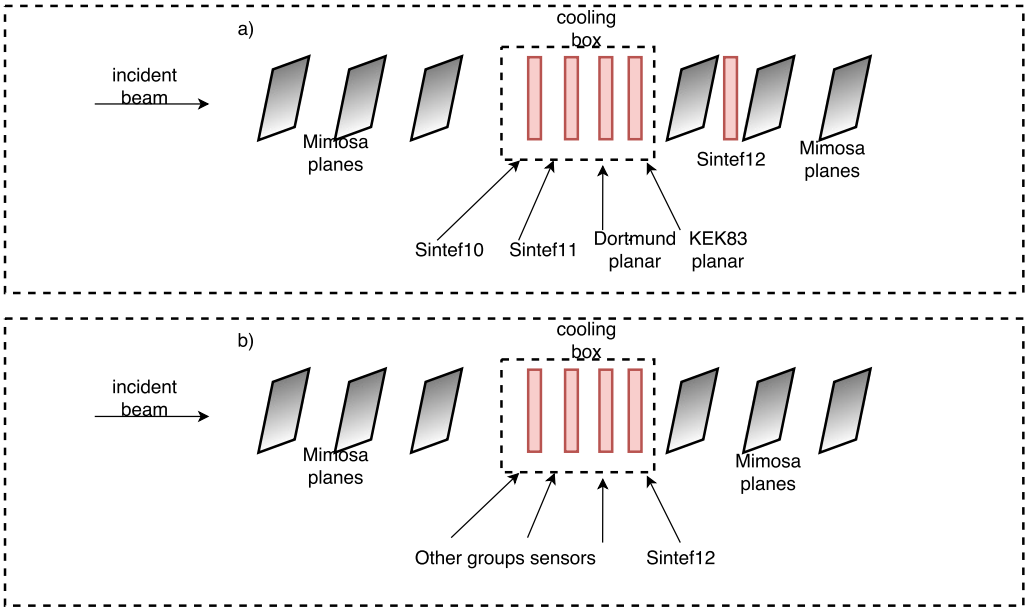

Figure 4.2: Placement of the SINTEF DUTs during the 2015 (a) and 2016 (b) testbeams. For the 2015 testbeam SINTEF 12 was placed between telescope plane 3 and 4 in order to see if we measured any difference due to the extra material in front of it. In the 2016 testbeam SINTEF12 was placed inside the cooling box in a configuration that allowed the very edge of the sensor to be hit by the beam. Note that the mimosa detectors are at a normal incidence angle with respect to the beam, and not tilted as the image may suggest.

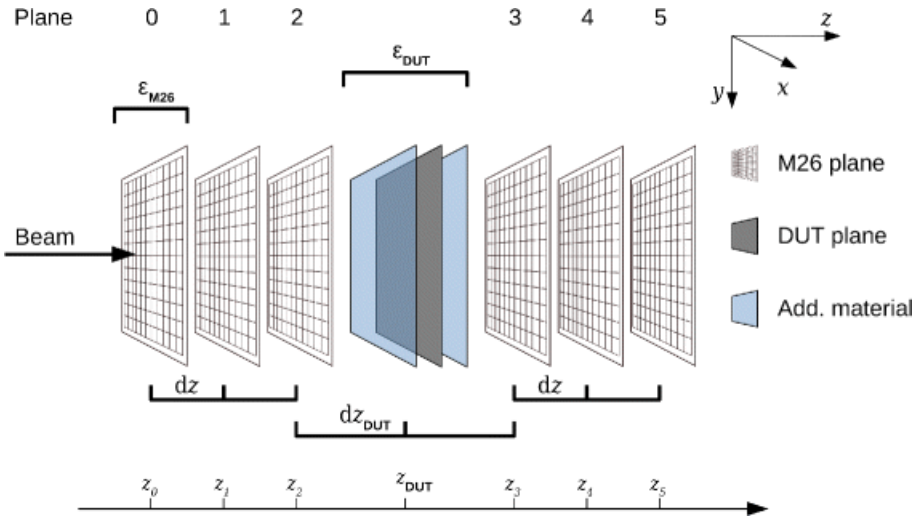

Figure 4.3: Schematic overview of the beam telescope setup. The variables ϵ_{M26} and ϵ_{DUT} are the Mimosa planes and the DUTs material budget respectively [35].

Hits in the pixels of DUTs have an uncertainty connected to them regarding what particle made what signal. The telescope is, therefore, a tool to provide true tracks of the particles that traverses the telescope and the DUTs, enabling efficiency

studies and track resolution studies of the sensors under investigation.

4.2 Testbeam Activities

The data analysed in this thesis were collected at two testbeams in the CERN north area testbeam facility. The first one was conducted in September 2015 and the second one in September 2016. Each of the testbeams provided good amounts of useful data.

The three SINTEF produced 3D silicon pixel sensors tested in the beam have electrode-columns penetrating the entire bulk thickness, and contain 336×80 pixels with pixel sizes of $50 \times 250 \mu m^2$ adding up to a total area of $16.8 \times 20 mm^2$. They were operated at several reverse bias-voltages and thresholds in order to perform systematic studies of the efficiencies.

In the September 2015 testbeam, all three SINTEF 3D pixel sensor prototypes were tested (SINTEF 10, SINTEF 11 and SINTEF 12). SINTEF 11 unfortunately had an area of damaged bump bonding and this area was left ineffective as a consequence. See Figure 4.4.

The goal of the testbeam in 2015 was to measure the sensors efficiency and spatial resolution. These studies were conducted at four different thresholds, which for each threshold three different bias voltages was tested. The threshold here refers to the threshold for the ToT set at 2000, 2500, 3000 and 4000 electron charges, with -5, -10 and -15 volts reversed bias voltage. A brief overview can be seen in Table 4.1.

In the 2016 testbeam we decided to test an irradiated sensor (SINTEF 11) as well as an unirradiated one (SINTEF 12) for edge efficiency studies. The irradiated sensor was irradiated in the proton beam of the SPS to a fluence of $5 \times 10^{15} n_{eq}/cm^2$. The top plot in Figure 4.5 shows the I-V characterization of the SINTEF 11 detector before irradiation, and shows a breakdown voltage (see Section 1.3.2) at approximately 20V. Generally we can see that the plateau starts at approximately 5V, which indicates full depletion already at low bias voltages. The bottom plot show the measured IV characteristics of the sensors during the testbeam in 2015, a few months before the top plot measurements. Here we can clearly see that SINTEF 10 is damaged as the leakage current is very high (NB! the y-axis are in log scale). The higher leakage currents in the two other sensors may stem from the fact that they were measured while assembled in the beam telescope and connected to an amperemeter situated a few meters away. While the later measurements of SINTEF 11 was conducted by Nicola Pacifico in a laboratory at CERN, within a controlled environment. In both cases the temperature was approximately room temperature.

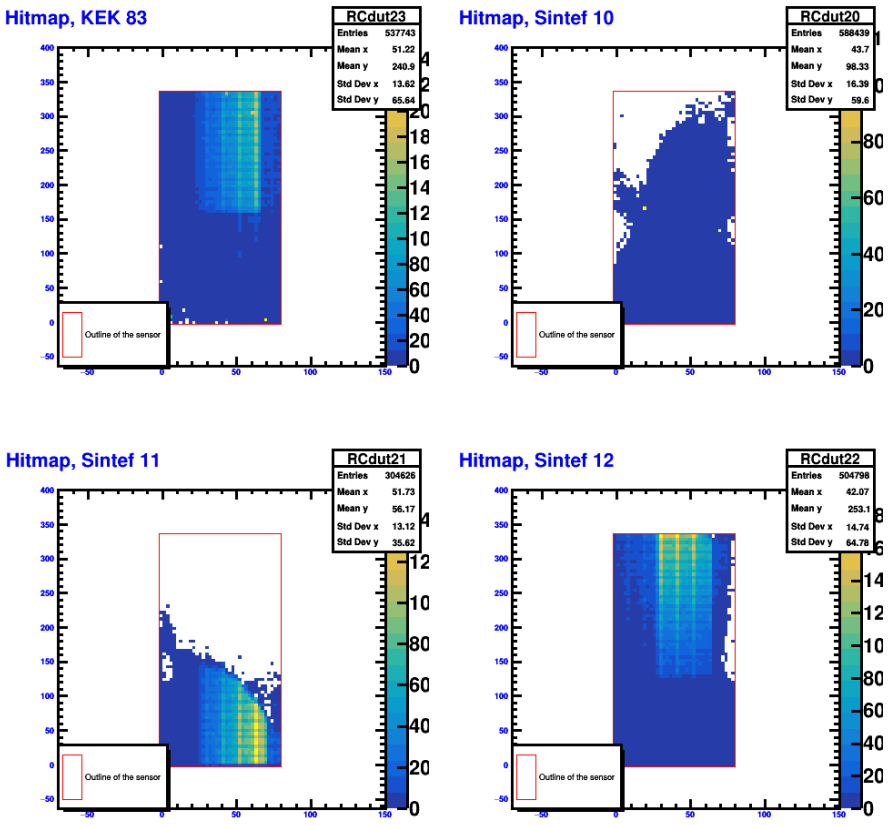

Figure 4.4: The plot shows the hits in the SINTEF 3D sensors as well as the Japanese KEK 83 planar sensor. The red square denotes the sensors area. The hitmap of SINTEF 10 and 11 shows large areas that are ineffective and not responding to any signal. This inefficiency were found to be caused by bump bonding damages. In the bottom right plot we see the SINTEF 12 hitmap where the square structure with more hits are the spatial acceptance area from the triggers.

SINTEF 11 show comparable characteristics in both cases.

After irradiation, during pre-beam tuning SINTEF 11 broke down and was rendered inactive, possibly due to a too high bias voltage and a short in the readout electronics. We did however get good amounts of data for the edge efficiency study with the working SINTEF 12 detector. The SINTEF 12 sensor was also this time operated at different bias voltages and thresholds.

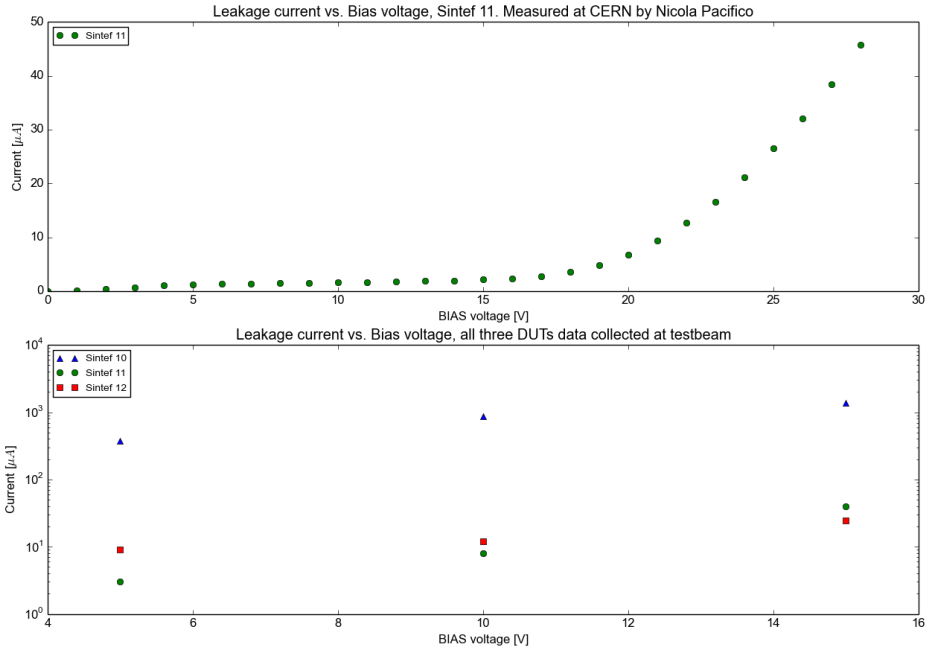

Figure 4.5: Top: IV curve of SINTEF 11, the breakdown starts at approximately 20V bias voltage and full depletion is achieved at approximately 5V. Bottom: IV characteristics of all three DUTs. The measurements were performed in the testbeam of 2015. The leakage current in SINTEF 11 was higher when it was measured in the testbeam (note that the y-axis is in log-scale).

Testbeam	DUT	Irradiation fluence	Threshold (electron charges)	Bias voltage (V) at threshold
2015	SINTEF 10	Unirradiated	2000, 2500, 3000, 4000	5, 10, 15
	SINTEF 11	Unirradiated	2000, 2500, 3000, 4000	5, 10, 15
	SINTEF 12	Unirradiated	2000,2500, 3000, 4000	5, 10, 15
2016	SINTEF 11	$5 \times 10^{15} n_e q cm^{-2}$	Broke down before testing	Broke down before testing
	SINTEF 12	Unirradiated	2000, 2500, 3000	5, 7.5, 10, 15

Table 4.1: Overview of the different thresholds and bias voltages used for the sensors during both the 2015 and 2016 testbeams. Note that for each threshold all the different bias voltages were used.

Chapter 5

Analysis

The data analysed and presented were collected over a total period of two weeks of data taking at the CERN north area testbeam facility. The analysis included an efficiency study both of the active edge and a general efficiency. Furthermore a study of the sensor's spatial resolution was performed and finally Monte Carlo simulations was made and showed comparable results. The Monte Carlo simulation procedure is described in detail in Chapter 6.

The general efficiency and systematic analysis of the efficiencies were done using the data taken in 2015 for three SINTEF sensors. While the edge efficiency analysis was done using the data taken in 2016 with only one pixel device (SINTEF 12).

The first step in any testbeam analysis is the actual acquisition of the data. In the EUDET-telescope the data are acquired using the EUDAQ software which are highly modular in the sense that it can support a range of readout boards compatible with the many different sensors that are tested in the telescope.

In order to have any knowledge about the real tracks of the particles through the telescope, and thus the impact points on the DUTs, these tracks needs to be reconstructed from the raw hit-data provided from the Mimosa planes. Reconstruction of the data used in this thesis were performed by Zongchang Yang and Bjarne Stugu using the EUTelescope reconstruction framework [36]. Both the 2015 and 2016 data were reconstructed this way.

5.1 Reconstruction Framework

The EUTelescope reconstructs the particle tracks event-wise, wherein each event goes through a series of processes; data conversion, clustering, hit making, alignment and fitting. Data conversion is the first step where the raw data from the telescope planes are converted into a standardised machine independent format synchronised with the information from the trigger unit. Additionally, the sensors are scanned for so-called *hot pixels*, namely pixels that have fired more often than the others indicating some kind of damage. This in order to exclude those pixels from the further reconstruction. For the Mimosa sensor only about 0.001% of the sensor area is defined as *hot* [37]. For the DUTs a hot pixel was defined as a pixel that had fired more than 1.5% of the time which resulted in approximately 5-10 pixels being excluded from each sensor. The data conversion serves the purpose of transforming hits into coordinates that can be read by a more general software.

The next step of the reconstruction is the clustering of hits. When a charged particle liberates electron-hole pairs in a pixel, the charge may drift and be collected at more than one electrode and thus give a signal in adjacent pixels creating a *cluster*. The identification of clusters are done in one of two ways; by fixed frame clustering or by a sparse clustering algorithm. The fixed frame clustering algorithm needs a predefined maximum size of the cluster, i.e. 3×3 or 5×3 adjacent pixels fired.

The sparse clustering algorithm works in a slightly different way. Sparse clustering algorithm can be subdivided into two versions, SP and SP2. The SP-algorithm demands that a adjacently fired pixel has a signal over some value for it to be considered a part of the cluster and not just noise. The SP2 algorithm have a spatial restriction, requiring a pixel to be fired within a predefined distance from the original pixel.

The third step is the "Hitmaking" step. In this process the local cluster coordinates (coordinates within the sensor reference area) are translated into a global coordinate system so that the fitter process may extrapolate straight lines for the tracks. In order to find the correct lines, an alignment are necessary.

The alignment is the process of adjusting the coordinates of the sensors a few μm relative to the hits. A study of the appropriate histograms and a manual alignment based on those yielded a better result.

Finally the fitting process fits the track-coordinates to straight lines based on the global cluster coordinates that are most likely to be correlated. These straight-line fits also gives the tracks through the DUTs. The points where these lines penetrate the DUTs, are known as the predicted impact points. The goodness of fit for the tracks can be evaluated by the χ^2-test described in Section 5.1.1.

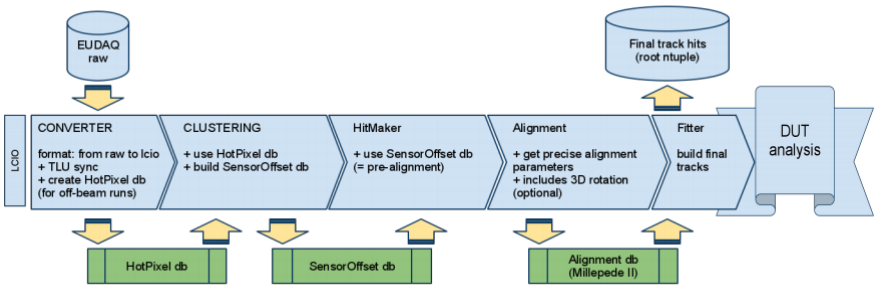

Figure 5.1: Flow chart of the EUTelescope framework. Between some of the processes a database from the previous step are exchanged (green boxes). After all the events have undergone the processes the DUT data are ready for analysis [37].

When all events have undergone the above-mentioned processes, the reconstructed tracks are put into n-tuples. N-tuples are files that contains an ordered structure of the data. Figure 5.1 shows a flow-chart representation of the five steps of the reconstruction.

5.1.1 χ^2 evaluation and post-alignment

An unbiased estimation of the goodness of fit is given by the χ^2 test. It can be used to evaluate experiments where there are ν independent variables x_i that are drawn from a normal distribution with mean μ_i and variance σ_i^2. The χ^2 test are given from [38] as

$$\chi^2 \equiv \Sigma_i^{\nu} \frac{(x_i - \mu_i)^2}{\sigma_i^2}. \tag{5.1}$$

In the reconstruction of the tracks several parameters are used and are known as the number of degrees of freedom ($ndof$) of the measurements. If the fraction $\chi^2/ndof$ is not too high, the fit is good. From Figure 5.2 one can see that the mean value of the χ^2 distribution from the telescopes reconstructed tracks average around 6 while the number of degrees of freedom are 8. This gives a $\chi^2/ndof \approx 0.73$ which is within the region for a good fit.

A $\chi^2/ndof$ value of < 5 was accepted for the Mimosa planes since the resolution and thus the χ^2 distribution is affected by the multiple scattering occurring throughout the telescopes length. When reconstructing tracks one needs to assume

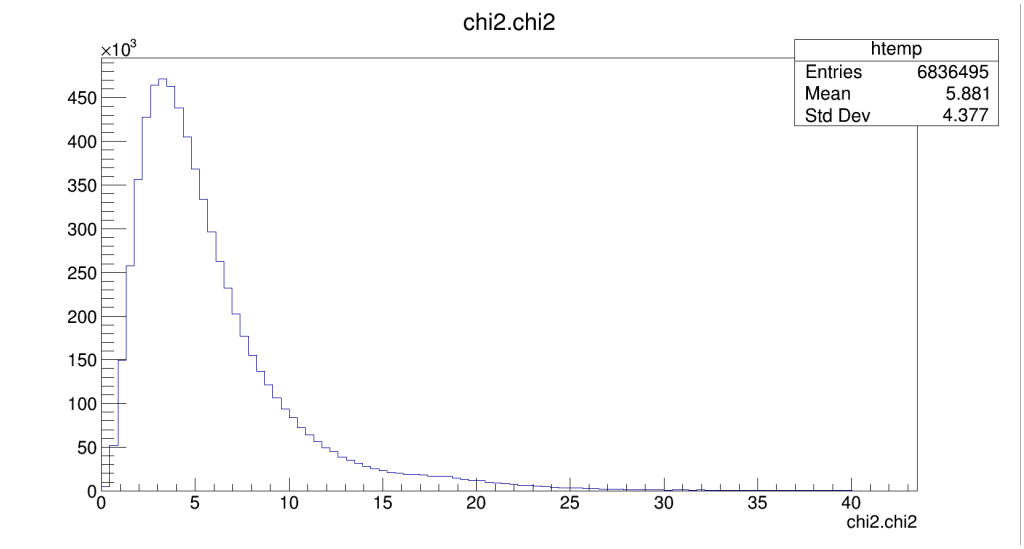

Figure 5.2: The figure shows the chi-square distribution of the reconstructed tracks from the reconstruction framework. The number of degrees of freedom are 8.

a spatial resolution for the telescope, after a manual alignment it was assumed to be $5.5\mu m$ as the χ^2 distribution had a too low mean for a coarser resolution assumption. Additionally, multiple scattering is taken into account when finding the χ^2 distribution.

In addition to this a threshold for the $\chi^2/ndof$ values for each track were set, and if the value were less than a certain value (i.e $\chi^2/ndof < 5$) the track was accepted.

5.2 Analysis Framework

The framework used to analyse the data was written by professor Bjarne Stugu some time ago, and developed further by prof. Stugu and the author, for this thesis. A simplified flowchart of the framework is shown in Figure 5.3 and the workflow is explained in the next few paragraphs.

The data is read and analysed event-wise, where each run is analysed separately. During the testbeam some groups may want to change their DUTs position or angle towards the beam. Therefore each run may contain slightly different positions and rotations of the DUTs, this is taken into account by an external script that applies the necessary corrections in. Additionally, each run is stored in separate files so that each run can be analysed separately. A brief outline of the workflow in the framework is given below.

First a few inputs are needed from the user in order to determine what kind of data (real testbeam data or simulated data) to be analysed. Whether to write efficiency maps to file or to read an already written efficiency map from this file is determined by the user. To be able to read the efficiency maps the user would need to run the script and write these maps to file first. Then run the script a second time in order to extract values from the file. When real data are chosen, the framework reads the NTuple files created from the EUtelescope reconstruction framework. All the tracks and impact points in the DUTs are stored in arrays with applied corrections to position and order, since this may have changed between runs. Furthermore, the clustering algorithm (explained in Section 5.2.1) is applied and returns the cluster sizes, cluster ToT etc. into the analysis. From here several further adjustments and rotations to the DUTs positions are done, this in order to get a better alignment.

In order to plot the efficiency and to reduce noise contributions from multiple tracks stemming from previous events, a strict requirement on the tracks is set. This cut is explained in Sections 5.2.2 and 5.2.3 and is set in the above-mentioned correction script. If the predicted impact points meet the requirements after the cut, the hitmaps used for efficiency maps are filled and divided by each other. The resulting efficiency map is exported into a separate file.

When all the events have undergone the aforementioned processes the framework is run once more, this time it reads the created file and extracts the efficiency values stored in the bins of the efficiency plot. Also checking each pixel that is hit in an event to see if it is "alive". If the pixel is "dead" then the pixel is excluded and the next event is analysed. These efficiency values are further used to plot more detailed information. Based on the information about the bias voltage and thresholds used during different runs, the systematic efficiency study can be performed.

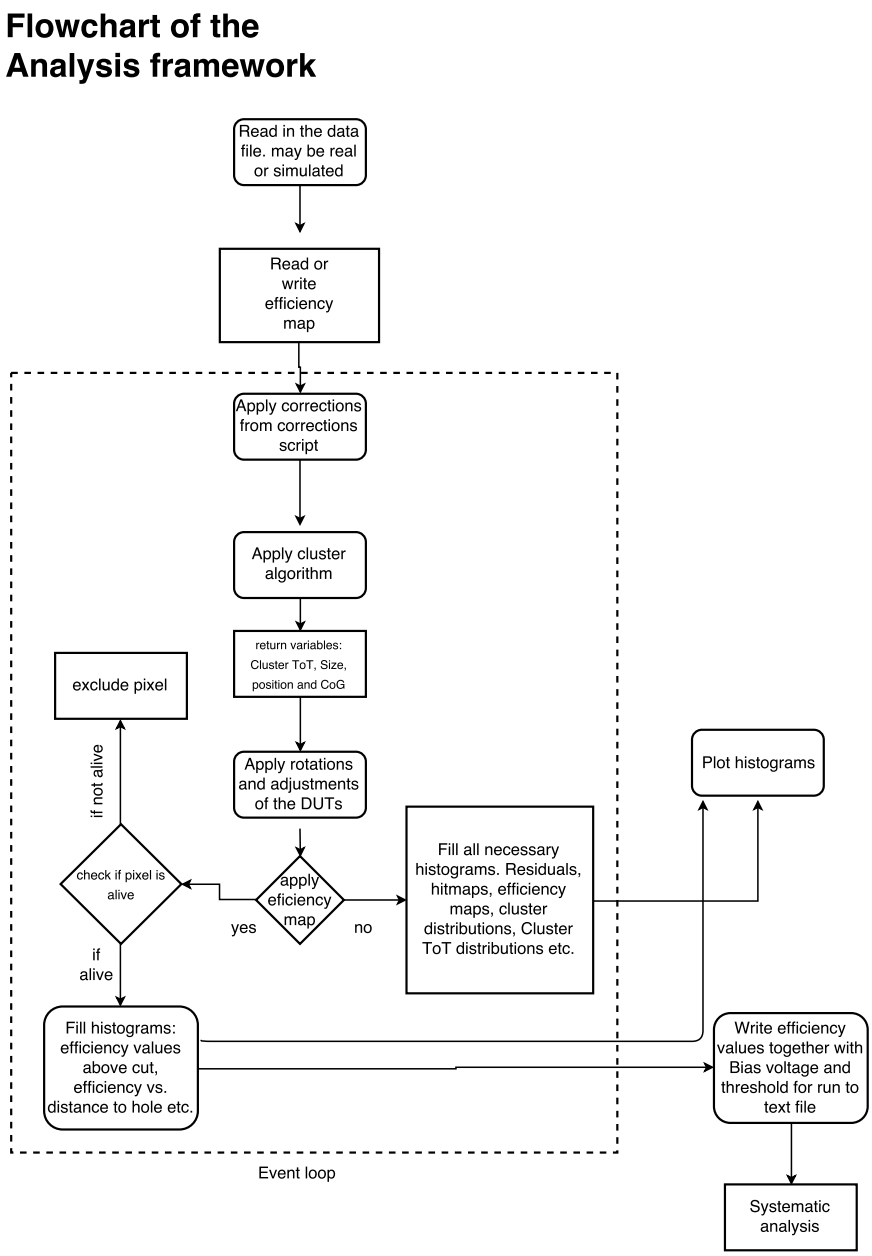

Figure 5.3: Flowchart of the analysis framework.

5.3 Analysis Results

The following sections will present and explain the results from the analysis of the data collected at the testbeam in 2015. The results presented here, use the data from two runs merged together. These runs were conducted with a threshold of 3000e and a bias of -5V with a tuning set to give a ToT count of 8 in response to a charge release of 20000e^- (tuning is denoted ToT=8@20ke). In addition, an

explanation of the clustering algorithm is given. This explanation is valid for every event analysis regardless of bias voltage or threshold since the clustering algorithm is an integrated part of the versatile analysis framework.

5.3.1 Time over threshold and clustering

The main goal of the analysis is to find the tracking efficiency and spatial resolution of the sensors we are testing. When measuring the efficiency of a sensor one finds the fraction of passing particles that are detected in the sensor. In order to find the efficiency of a sensor the number of hits that created a cluster are counted and not the individual pixel hits. As the liberated charges drifts in the silicon, some may be collected in adjacent pixels thus introducing an uncertainty as to where the particle passed. This is illustrated in figure 5.4. Therefore the first step in the analysis is to create clusters based on the ToT distributions provided in the input data. The distribution of the ToT, should follow a Landau-type distribution due to the proportionality to the energy deposition. However, the amplification and the capacitors discharge rate can affect the distributions as well as any damage in the electrodes or pixels. Additionally, the DUTs are tuned to a certain ToT based on the charge released, for instance one tuning could be such that a charge release of 16ke^- should yield a signal with ToT = 8. The tuning is done before the data taking is started and the common convention is to create several configurations of the tuning. This way it is easy to change the DUTs response inbetween runs. For the runs that gives the results below a tuning of 20ke^-@8ToT is used. The distribution for the largest ToT in each of the sensors is shown in figure 5.5.

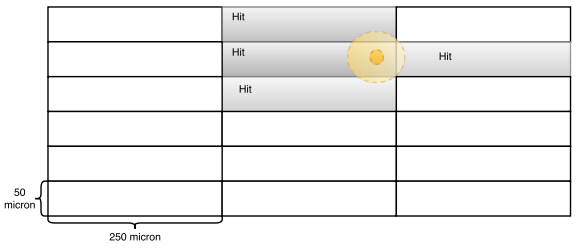

Figure 5.4: Illustrates of how charge liberated from a passing particle is shared between the neighbouring cells that give rise to a signal in adjacent pixels. It is also apparent that the amount of charge collected in each pixel differ, hence the ToT also differs for the pixel cells.

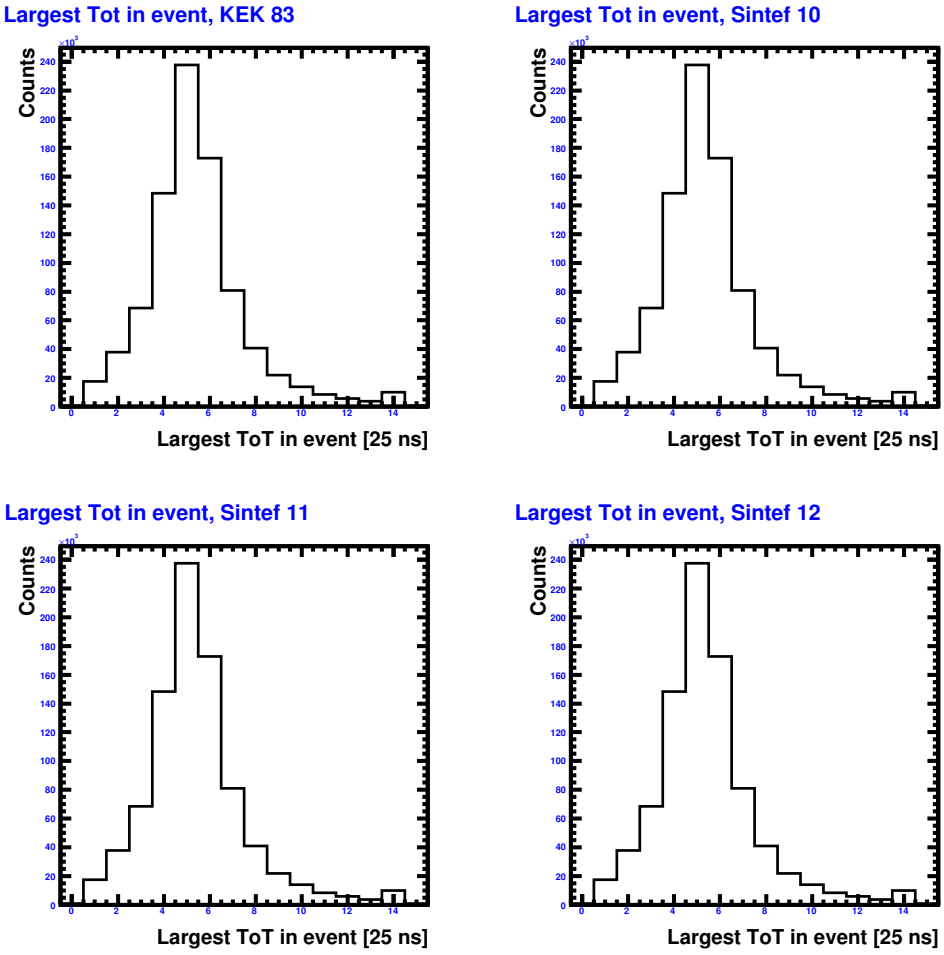

Figure 5.5: The plots show the largest time over threshold distributions for the DUTs SINTEF 10, 11 and 12 as well as the Japanese KEK 83 planar sensor.

The clustering algorithm used for the DUTs works in the following way:

1) The pixel with the largest ToT is found, called seed pixel, and surrounding pixels are scanned for hits. This check have no spatial restriction and extends all the way to sensors edge if necessary.

2) When a neighbouring hit is found it is added to an array that keeps track of the hits local coordinate and its ToT.

3) When all hits are collected they are returned into the rest of the analysis framework with the local coordinate for each cluster member, the centre of gravity (CoG) position (Eq. 5.2) within the cluster, and the summed ToT of the cluster.

The centre of gravity is based on the cluster charge distribution, where the

cluster center is given by

$$x_{cog} = \frac{\Sigma_i Q_i x_i}{\Sigma_i Q_i}, \tag{5.2}$$

where Q_i denotes the individual charge collected in pixel i and x_i is the pixel coordinate. The center of gravity algorithm is the most widely used algorithm to find the centroid of a cluster, and it is this position that is referred to as a hit in a DUT unless otherwise specified.

In figure 5.6 the distribution of the total ToT of the clusters is shown. Here the ToT of each individual signal in a cluster are added on top of each other. If comparing Figures 5.5 and 5.6 one can see that the peak of both distributions lie between 5 and 6, indicating that the particles have deposited most of their energy in the seed pixel. Furthermore, the plots in Figure 5.6 shows a small tail on the left side of the peak for the SINTEF detectors, most prominent in SINTEF 12. These tails are due to the electrode "holes"[1] reducing the amount of charge that is collected and thus the ToT of the cluster. Additionally, we can see that the KEK83 detector plot shows no tail, which is due to this detector's planar electrode layout.

The statement of energy deposition mostly inside the seed pixel is backed up by the plot of the cluster sizes, seen in Figure 5.7. In this figure we can see that most clusters are only one pixel large indicating an energy deposition in one pixel cell only.

Furthermore we can plot the distribution over how many cluster we find in a sensor stemming from the same event. This is shown in Figure 5.8, where we can see that it is mostly only one cluster found for each trigger and only a few triggers provide us with 2-3 clusters. More than one cluster per trigger may hint at noise in the detector since the probability of having two particles traversing the detector at the same time is low. The counts of zero clusters are due to tracks in the telescope that do not hit our DUT, or the predicted impact points lie in a damaged area of the DUT. This becomes apparent when observing SINTEF 1's cluster multiplicity distribution, and recalling that SINTEF 11 had a very large ineffective area.

[1]The term "holes" is used here because the electrodes penetrate the entire bulk thickness, and the particles enter the detectors at a normal incidence angles thus the electrode looks like a hole for the particles.

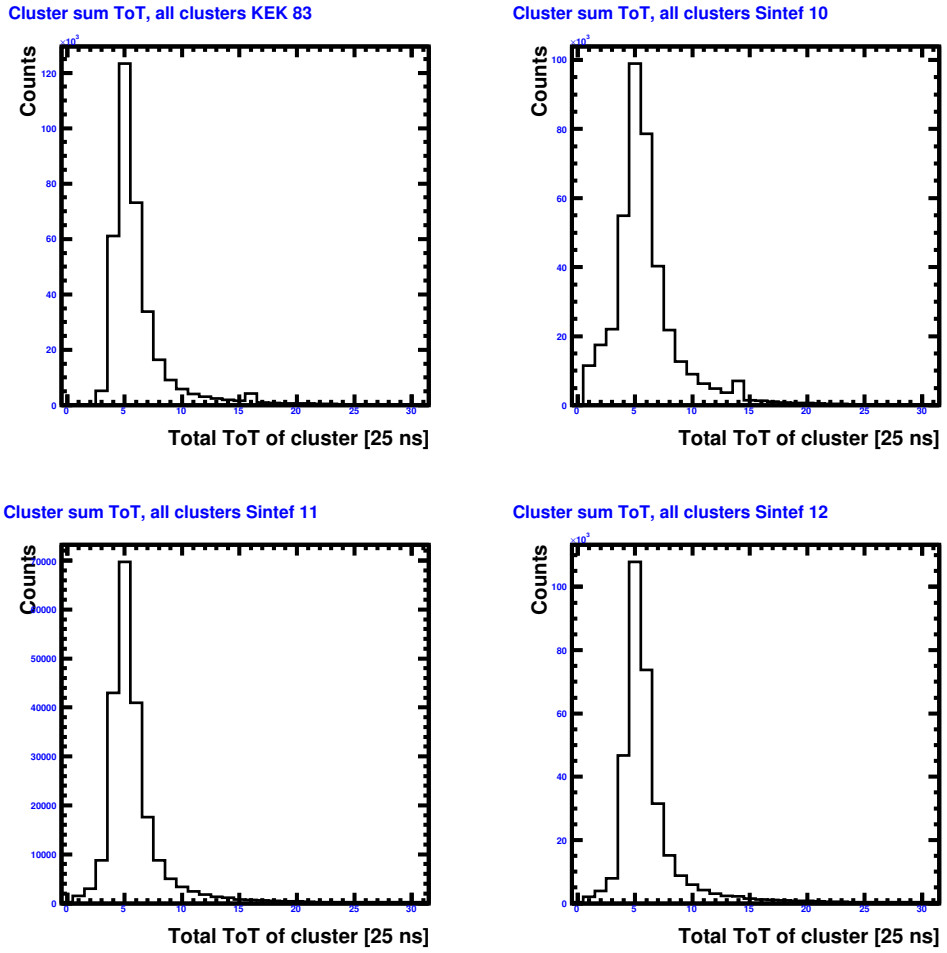

Figure 5.6: Distribution over summed ToT in the clusters.

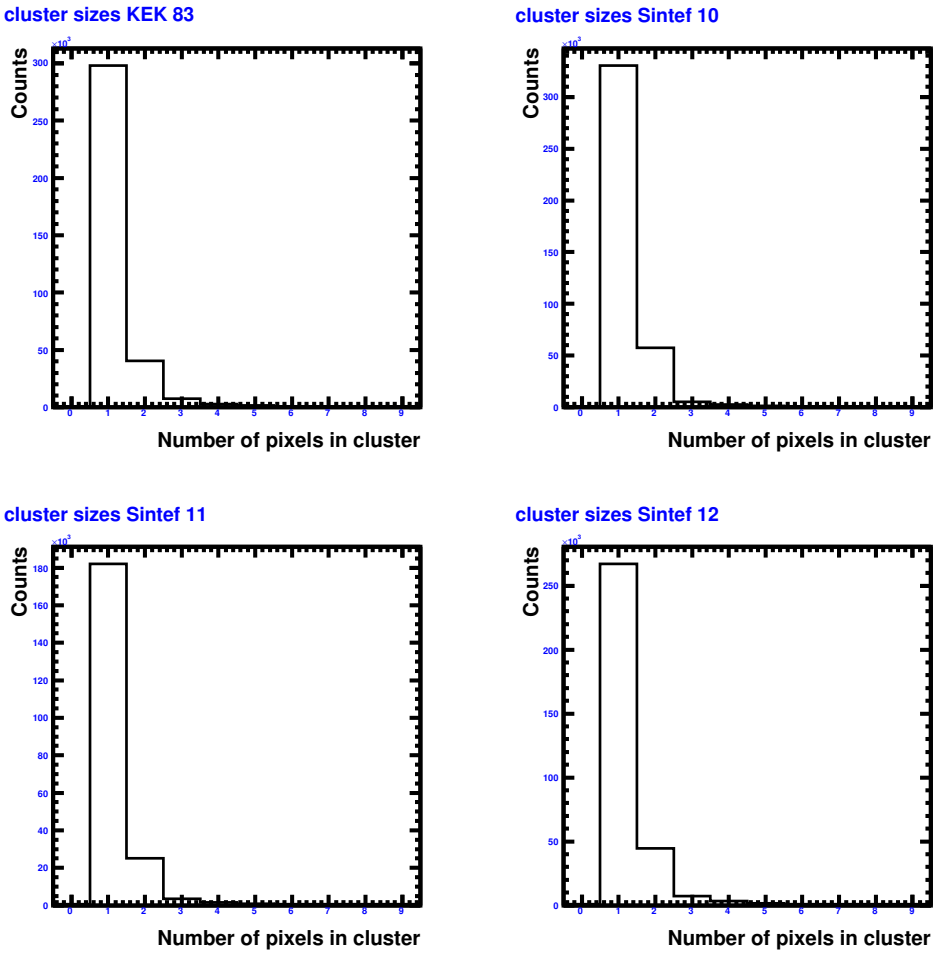

Figure 5.7: The plot shows the cluster sizes in the four DUTs.

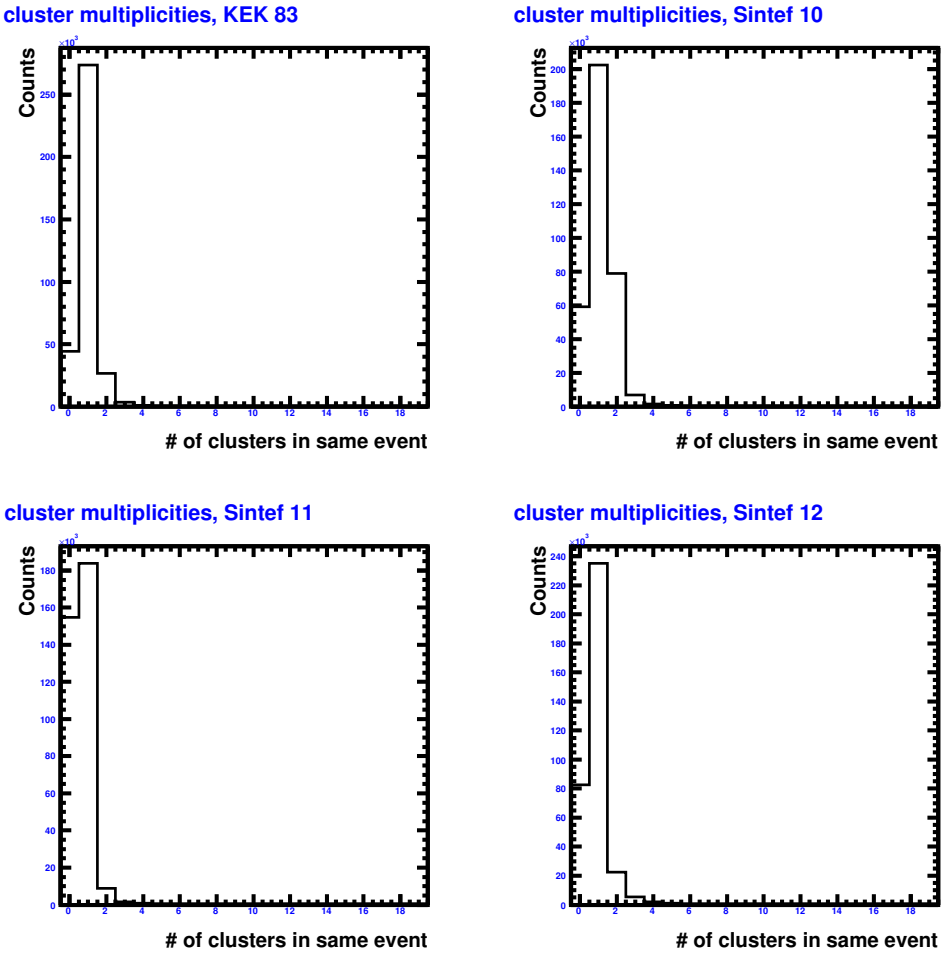

Figure 5.8: The plot shows the cluster multiplicities for each of the DUTs. The distribution is centred around 1 which implies that mostly only one cluster is found for each trigger.

5.3.2 Sensor resolution

Further analysis requires the hits made in the DUTs to be aligned with respect to the telescope. This is done by applying rotations and adjustments in the analysis framework after the cluster properties are found. The distance between each hit in the DUT and the predicted impact point from the telescope is known as the residual of the track. By reducing this distance, a better alignment is achieved. Figure 5.9 shows the distribution of residuals for SINTEF 12. We can see that the residuals are distributed about 0 in both the x and the y directions. This distribution should of course only have a sharp peak distributed around 0 and extended out to the pixel size in the respective dimensions if the resolution were perfect. Multiple scattering and other effects contribute to the smearing of the distribution.

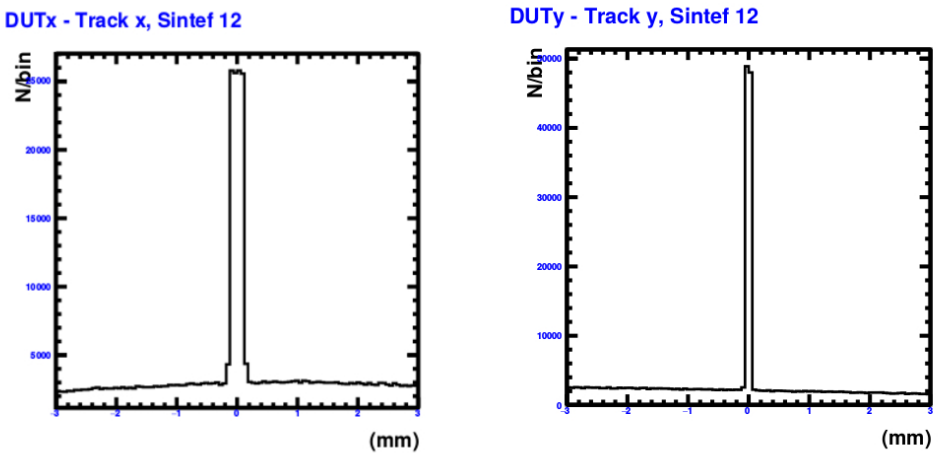

Figure 5.9: The distribution of residuals in x and y directions for SINTEF 12.

When the alignment is satisfying one can find the spatial resolution of the DUTs. This is done by fitting the residual distributions and finding the smearing of those distributions. The resulting plots are shown in Figures 5.10 and 5.11, where the distributions are fitted with a box function convolved with a Gaussian in order to smear out the edges to fit the distribution.

We can see that in these plots, the distribution have a flat peak around the pixel size in the respective dimensions but smeared out to some extent. The FWHM gives the pixel size in the respective direction since the peak are smeared out, and cannot be associated to a pixel dimension directly. Zero are taken to be the center of the pixel so the distribution should be box shaped and extend $\pm 125 \mu m$ and $\pm 25 \mu m$ in the x- and y-directions respectively, if a perfect resolution is achieved. Furthermore, the smearing gives the resolution of the sensor and this value is given by the standard deviation (σ) of the fit. A better resolution in y-direction is expected since the pixel size is only $50 \mu m$ in the y-direction, compared to $250 \mu m$ in the x-direction.

However, the resolution in both directions can be improved by introducing a cut that suppresses the noise from various sources. This is realized through the use of a reference sensor.

Some events can still be contained in the buffer of the telescope readout when a new event is measured in the DUTs. This impose a problem when determining the actual track through the DUT. This effect is important to account for in the resolution study, but also when measuring the efficiency (Section 5.2.3) since the measured number of tracks is larger than the actual number of tracks in an event, due to this event delay. By demanding that any track that passes through the DUT also passes through a restricted area in the reference sensor, the noise contribution from the delayed events is suppressed. In addition noise contributions from electronics and multiple scattering are reduced hence the resolution improves with the cut. The error in the resolution measurements are obtained from the fit which may be misleading for runs that contain low statistics.

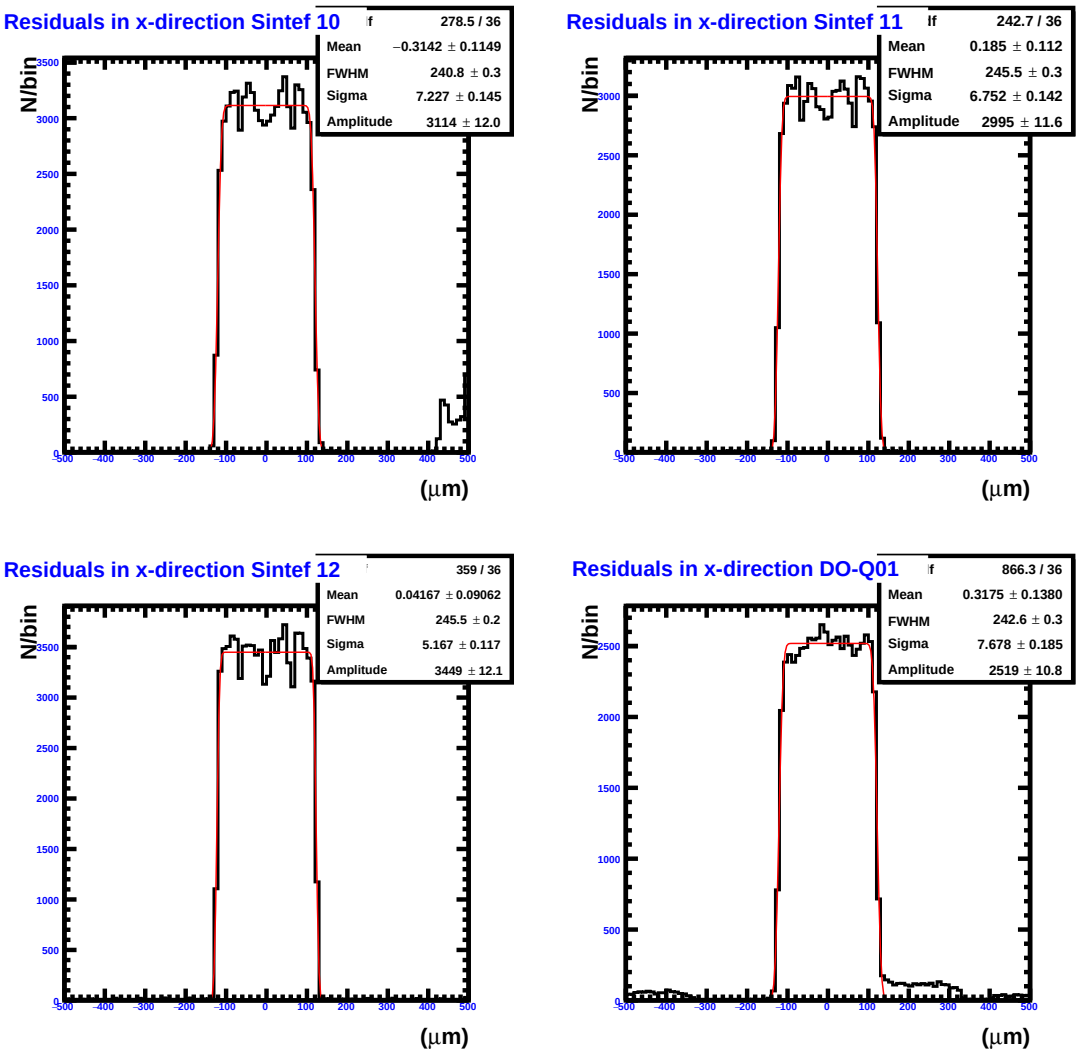

Figure 5.10: Residuals distribution in the x-direction with each track associated to a reference sensor. The plots are fitted with a box-Gauss convolution. The "Sigma" parameter is the standard deviation of the Gaussian and give the resolution.

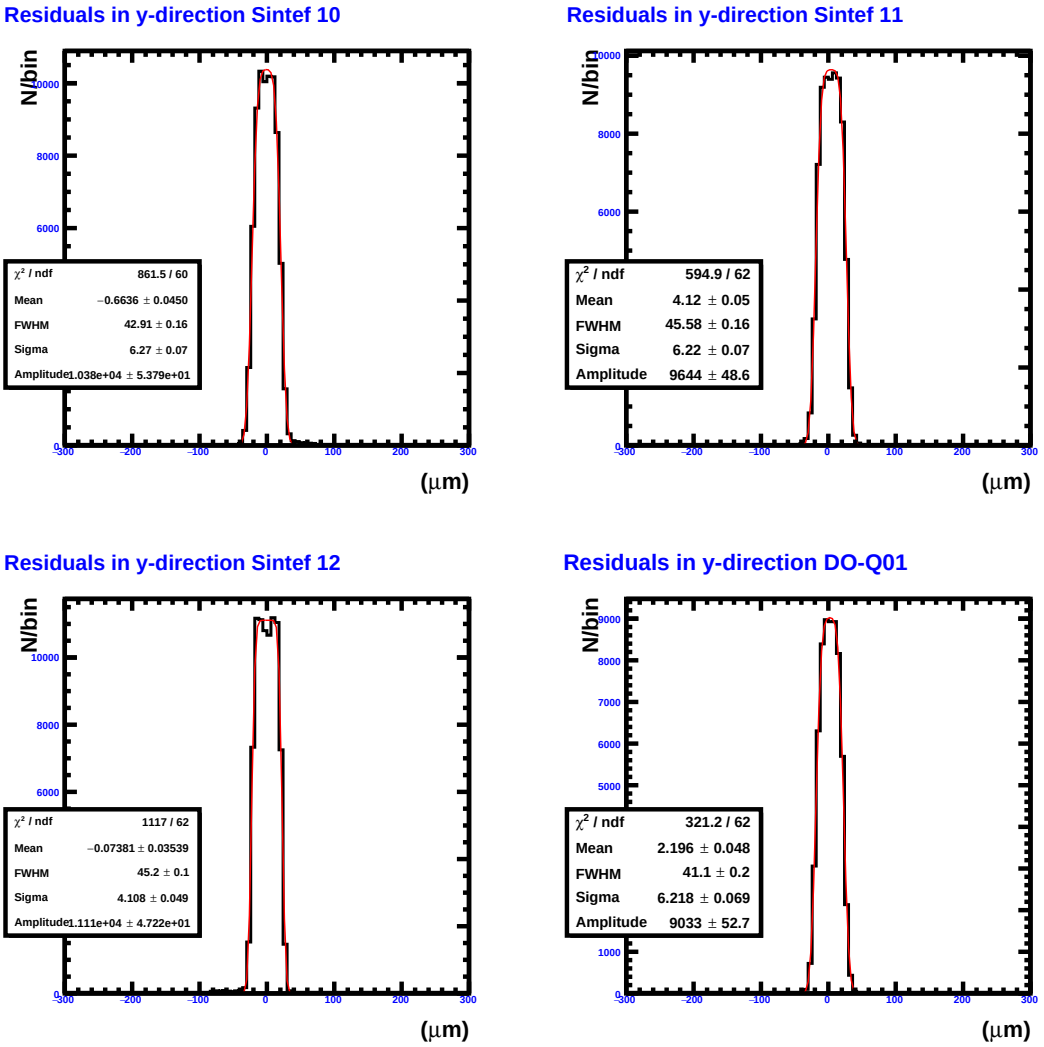

Figure 5.11: Residuals distribution in the y-direction with each track associated to a reference sensor. The plots are fitted with a box-Gauss convolution. The "Sigma" parameter is the standard deviation of the Gaussian and give the resolution.

Another interesting feature can be seen in the flat plateau of the distributions of the residuals. Here several dips are seen which are consequences of the electrode columns in the detectors. These electrodes show a significant drop in detection efficiency, and thus the tracking of a particle in this region is less optimal giving rise to these dips. For the residual distribution of the Dortmund detector DO-Q01 no such dips are seen which is due to its planar geometry.

5.3.3 Sensor efficiency

Another goal in the characterization of new detector technologies is to find the tracking efficiencies. These efficiencies are a testament to the design of the pixels as well as the geometry and placement of the electrodes. Since the electrodes in a 3D pixel geometry penetrates the entire bulk, the efficiency will suffer as a result. This is mainly due to the drift-diffusion mechanisms in the heavily doped electrodes. The electrodes are too heavily doped to be fully depleted and no electrical field is present, as such the charge carriers are transported by diffusion here. For a signal to be detected on the electrode the charge needs to move, and since no electric field are present to move the charges inside the electrodes, little to no signal are collected. The random movement in the diffusion of charge carriers may contribute a little bit to the signal, hence some efficiency is measured but it is much lower than in the other regions of the pixel.

For plotting the efficiencies some cuts and conditions are set. In order to get the efficiency a spatial restriction is set around a track in a reference detector, similar to what is described for the spatial resolution measurements. Accepting a hit in the DUT as a real hit demands that the track that passed through the detector also passes through a restricted area (window) of the reference detector defined in the analysis code. Furthermore, since the efficiency is given as the fraction of particles producing a hit in the sensor to the actual number of particles passing through the detector, two histograms are needed. Histogram 1 is filled with tracks that both yielded a hit in the DUT *and* was within the restricted area of the reference sensor. Whereas histogram 2 is filled with tracks that are contained in the full detector area of the DUT. By dividing histogram 1 with histogram 2, each bin in the plots are divided and yields the efficiency (Figure 5.12).

By changing the size of the window in the reference sensor the efficiency changes as well. This is investigated in detail in Section 5.2.4 in order to find the optimal size of the window that yields the optimal efficiency.

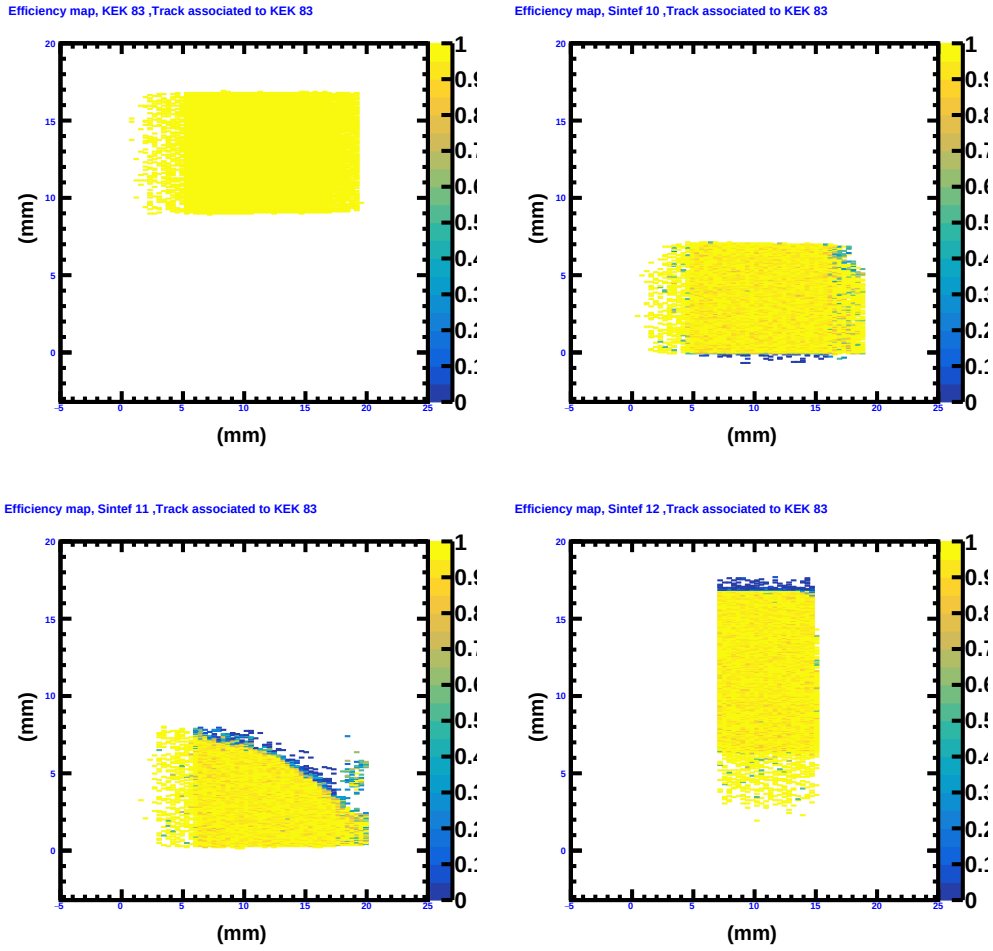

Figure 5.12: Tracking efficiency of the DUTs with tracks associated to a window in the reference sensor KEK83. Yellow indicates 100% efficiency

In Figure 5.12 we can clearly see the reduced efficiency in SINTEF 11 due to the bump bonding damage. For KEK83 100% efficiency are as expected since the histograms used to produce the KEK83 plot are identical (the detector is its own reference). The window cut does not affect its efficiency as the tracks in that sensor will always fit inside the defined window of this sensor. These plots however, does not yield any more than a visual representation of the efficiencies, and in every case the numerical value of the overall efficiency is of interest. Each bin in the plots in Figure 5.12 is representing one pixel and thus the plotting of each bins efficiency value are justified as a means of extracting the overall efficiencies of the detectors.

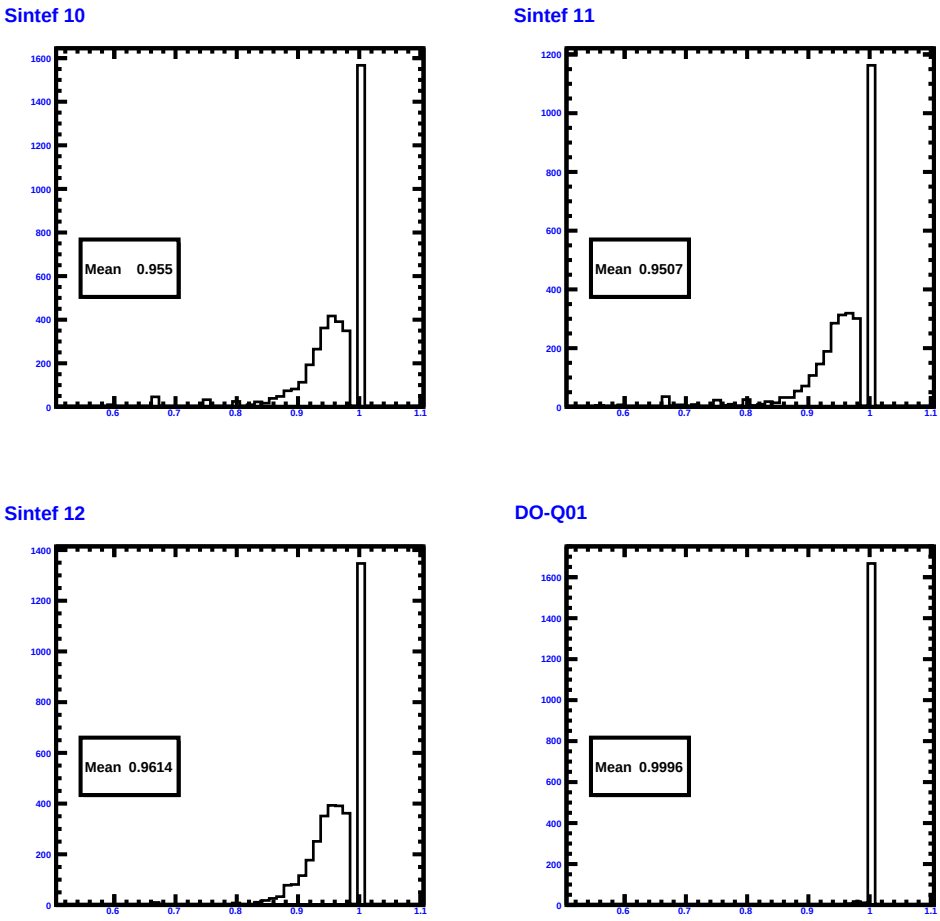

Figure 5.13: The histogram shows the count of bins (pixels) with an efficiency value associated to them. the DO-Q01 sensor shows just below 100% efficiency which is due to the planar geometry of the sensor and no ineffective electrode holes.

To find the numerical values an additional plot is made where a new cut is applied. First the bins in the plots of Figure 5.12 are extracted and their numerical values (the efficiencies) are stored in an array. Then these values are plotted as a one-dimensional histogram with a cut that excludes efficiency values of 50% or less.

This in order to exclude the low-efficiency electrodes from the calculation. Figure 5.13 shows this efficiency distribution.

Figure 5.14 shows the efficiencies superimposed into one pixel area with the reduced electrode efficiency clearly visible.

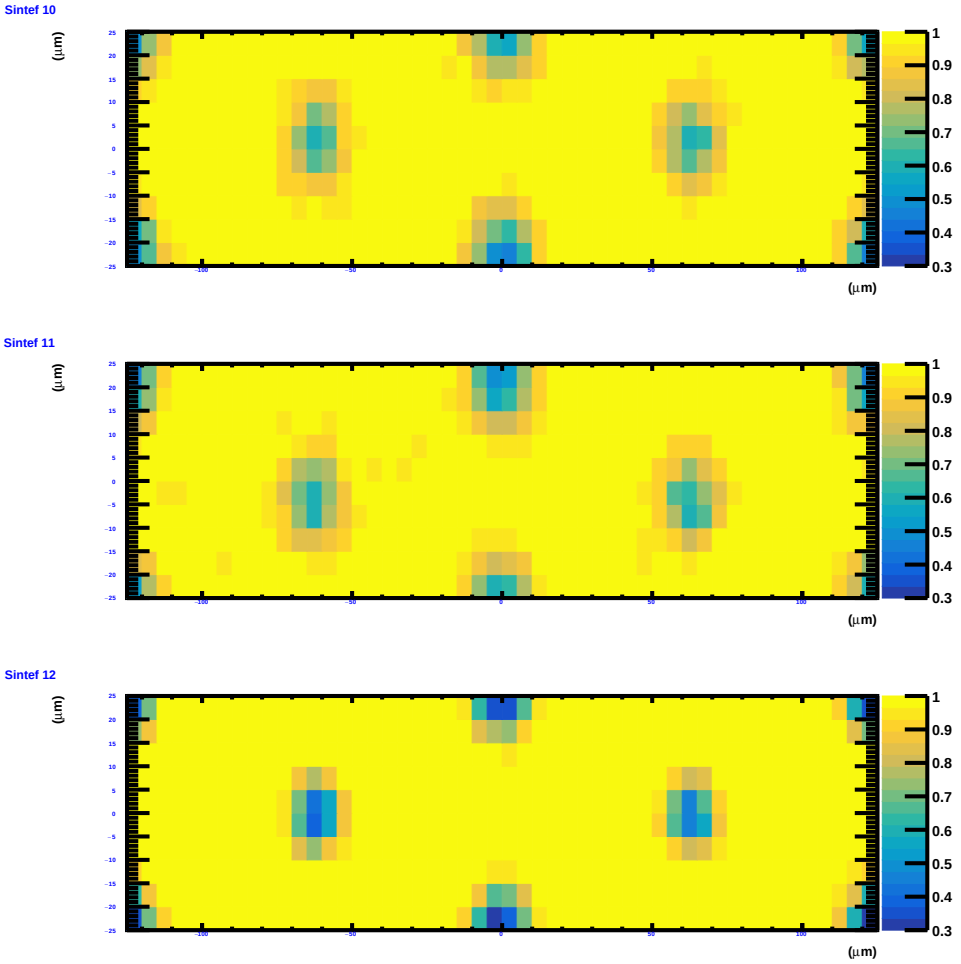

Figure 5.14: The plot shows the lower efficiency in the electrodes by superimposing the entire detector efficiency onto one pixel cell. Well visible are the edge electrodes as well as the two center readout electrodes yielding a lower efficiency.

From Figure 5.14 we can see that the efficiency drop below 50% are located within the electrodes ($r = 7\ \mu m$) although a more detailed binning is needed in order to determine how far the efficiency drop extends outside the electrode area. The DUTs are placed at a normal incidence angle with respect to the beam and some particles may hit only the electrodes thus a very small signal is collected. Figure 5.15 shows how the charge collection would look like for a small-angle tilt with respect to the beam. Then the particles that hit the electrodes would not ionize mainly inside the electrode columns but also somewhat in the depleted material between them.

This would increase the efficiency of the detector.

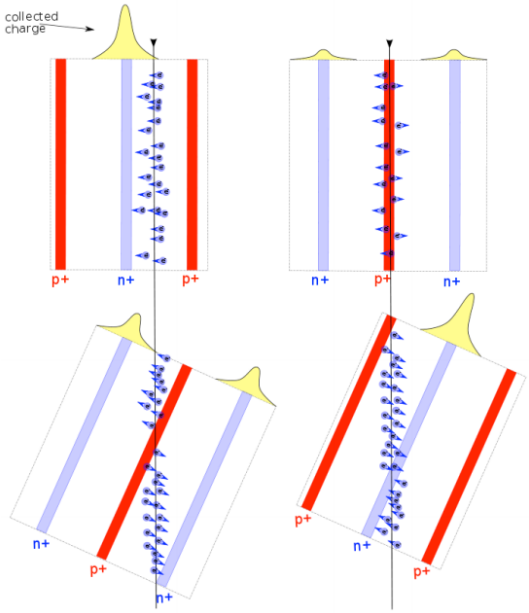

Figure 5.15: The image shows how the charge are collected when the sensor are tilted to some degree with respect to the beam. This tilt should show an increase in efficiency due less ionization inside the electrodes [39].

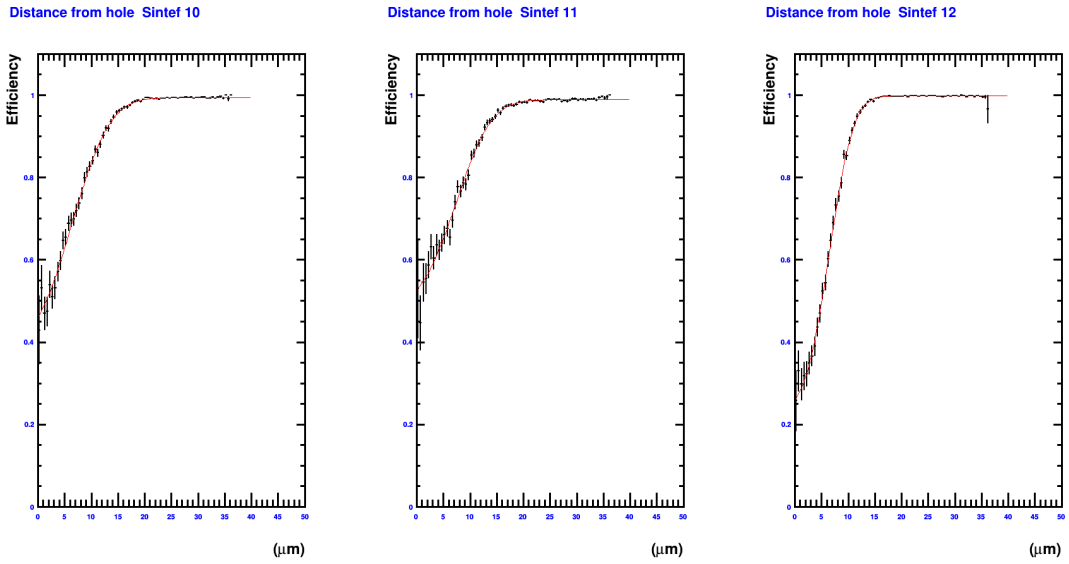

Figure 5.16: The figure shows the efficiency as a function of distance to the nearest hole. The efficiency profile is fitted with a step function convolved with a Gaussian function. As can be seen the efficiency is very close to 1 outside the hole region

As explained above, the charge transportation inside the electrodes are governed by diffusion due to the low electric field strength, thus a lower signal is collected there. Figure 5.16 shows the efficiency as a function of distance to the nearest

electrode. It is fitted with a step function convolved with a Gaussian and show an efficiency of 40% in the holes. Furthermore, the efficiency inside the holes seems to follow a step function and the efficiency plots in Figure 5.16 are smeared out due to the track resolution. For SINTEF 12 one can see that the shape is much steeper which is due to the better predicted impact points (better alignment) in the detector.

5.3.4 Systematic studies of efficiencies

The efficiency results depicted in the previous sections are all taken from one data file with one threshold and one bias voltage, therefore the results may not be indicative of how the sensors actually perform when put into use. Thus an systematic study was performed in order to learn what impact the bias voltage and the thresholds have on the efficiency.

By extracting the mean efficiency of the DUTs for each run and plotting this against the used bias voltage in the run, we can see how the bias impacts the detection efficiency (Figure 5.17). We also observe a somewhat expected behaviour of the efficiency response to the bias voltage at each threshold with increasing efficiency for higher bias voltages. From these plots it is apparent that SINTEF 12 is the best performing sensor during the testbeam. The uncertainties in the measurements are collected from the histograms used to plot the numerical efficiency values (Figure 5.13) where the uncertainty is calculated according to Eq. 2.19.

Furthermore, we observe that SINTEF 10 starts to show an unwanted response at approximately 3000e threshold. This was understood to be an effect of SINTEF 10's high leakage current (Section 4.2, Figure 4.5) and this is shown in Figure 5.18 where the efficiency of SINTEF 10 remain the only sensor to show an increase in efficiency at higher threshold even though this is expected to reduce the efficiency.

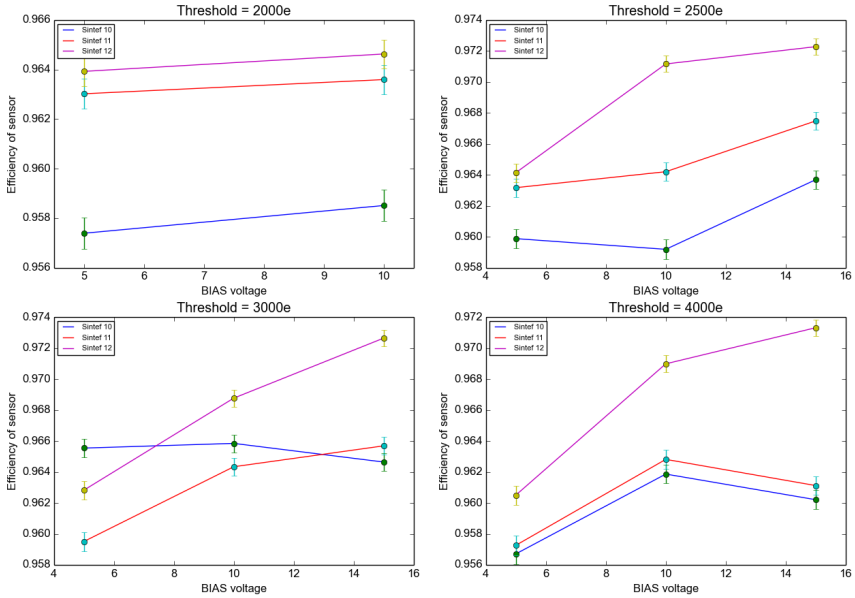

Figure 5.17: The plot shows the efficiencies as function of the bias voltages used.

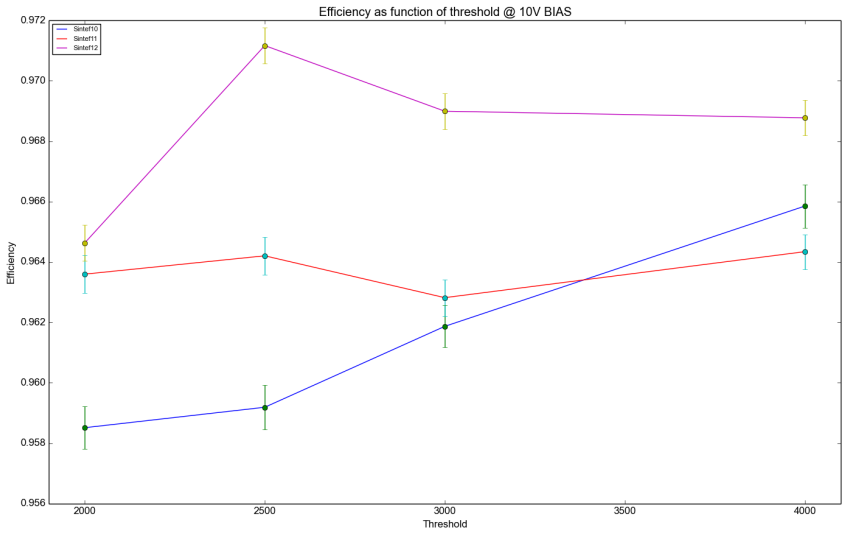

Figure 5.18: Systematic plot of efficiency vs. threshold. SINTEF 10 deviates from the expected behaviour.

5.4 Active edge characterization

In the 2016 testbeam two main goals were set; study the active edge of the sensor and test an irradiated device. The irradiated device broke down (Section 4.2) and was not tested. The tuning for SINTEF 12 was set to give a ToT=9 for a charge release of 20000e.

The data for the edge efficiency were collected by placing the sensor such that the beam only coincided with the very edge of the active area. Figure 5.19 shows how the beam was intercepted by the detector area. The square containing more hits represents the trigger area of the beam.

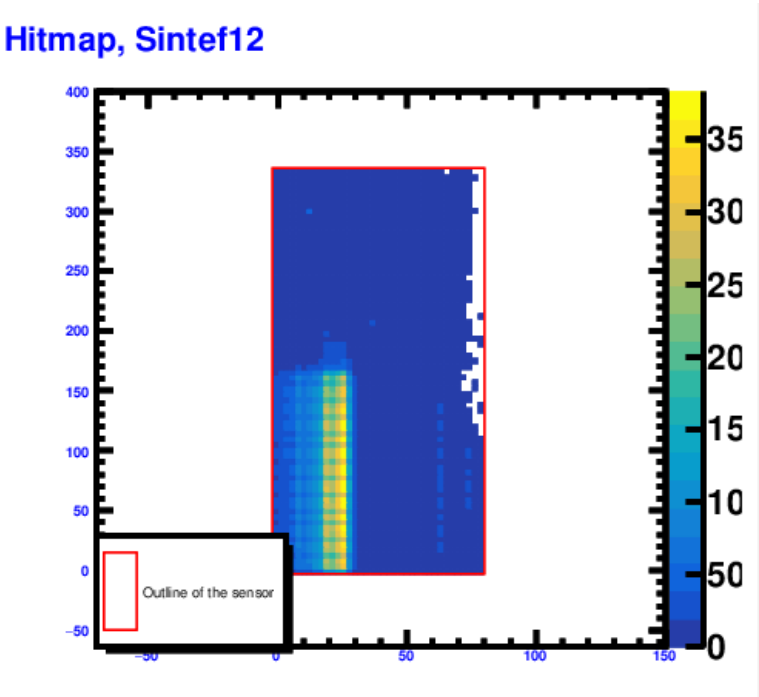

Figure 5.19: Hitmap of SINTEF 12 with a beam intercept at the sensors edge.

The method of extracting the efficiency from the active edge measurements is similar to the one as explained in Section 5.2.3. However, since the beam is intercepted only by the very edge of the DUT, the demand on what hits to accept must be changed. Instead of only demanding that the track passed through a window in the reference detector, all the hits on the edge are collected. This is done by choosing the zeroth pixel as the measuring point, that is requiring a hit in the zeroth row or column. Further, if a track passed through the window of the reference sensor the predicted impact point is checked to see if it lies on the DUTs edge. This is checked individually for the x and y direction where all hits in a row or a column along the entire DUTs edge are checked for hits. If a hit is found it is added to its respective histogram. This way only hits produced in the sensors edge are selected

and superimposed onto the zeroth pixel to yield more statistics.

Another nice feature of choosing the zeroth pixel is that we get measurements of the active edge in both directions simultaneously, while choosing a pixel that lies in the middle of the first row would only yield measurements of the active edge in one direction. In Figure 5.20 the plots of the efficiency in the active edge are shown. These plots are fitted with different functions due to the large noisy area seen in the y-directional plot.

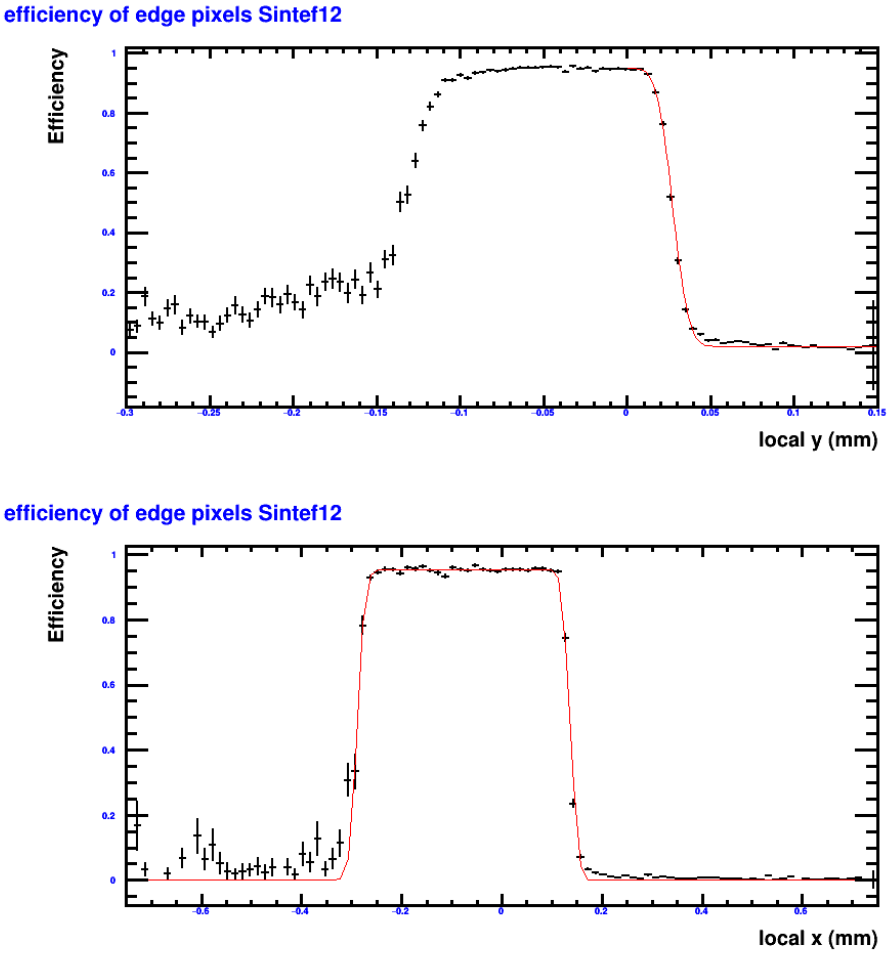

Figure 5.20: Edge efficiency in both directions. All the efficiency are collected into one pixel cell to increase statistics. Zero is the edge pixels center and the right side of the plots is inwards into the sensor.

In both plots the right side is the direction into the sensor and 0 is the edge pixels center while the left side is outwards from the sensors edge. The top plot show the efficiency of the active edge in the y-direction, i.e the direction towards the large empty are seen in Figure 1.8. On the left side, out from the edge, a certain efficiency are still measured. This is due to depletion from the edge electrodes extending a bit

further than the pixels edge outwards from the sensor and an electric field is present. Therefore when a particle hits this area the liberated charges drifts toward and are shared between the edge electrodes accumulating more charge than expected, such that the effective pixel size increases. This can also be seen in the plot for the x-directional edge, but to a much smaller extent due to the smaller area between the active edge and the bias ring. The fit used for the top plot in Figure 5.20 is a step function convolved with a Gaussian and fitted only on one side due to the smearing of the efficiency outwards from the sensor. In addition the bottom plot is fitted with a box-Gaussian convolution due to the smaller smearing of the measurements. The errorbars are calculated by applying Eq. 2.19 to each individual bin.

5.5 Summary of the Analysis

The particle tracks were successfully reconstructed with the EUTelescope reconstruction framework. However, the alignment of the DUTs needed some modifications in order to get good results, this was done offline. With the predicted impact points from the beam telescope, ToT and cluster distributions have been made. These show that most of the energy is deposited in the seed pixel. Furthermore, from a fitted distribution of the track residuals, a resolution have been found to be approximately 5-7 μm for the three DUTs tested in 2015. The same DUTs show a charge collection efficiency above 95% with SINTEF 12 showing an efficiency above 96%. The efficiency has been systematically studied for all the different thresholds and configurations used during the testbeam. In these studies we observed that SINTEF 10 had a deviation from the expected behaviour, which is most likely due to the high leakage current observed in the IV-characteristics.

The active edge characteristics has been investigated in data collected from the testbeam in 2016 for SINTEF 12. This analysis show efficiency well beyond the nominal edge of the sensor, stemming from a depleted region that extends outwards from the edge electrodes.

Chapter 6

Testbeam Simulations

In a testbeam experiment many factors affect the measurements, for example the damaged sintef 10 detector show a large ineffective area and a high leakage current thus a characterization of this detector becomes very hard. By using Monte Carlo simulations to resemble the real world as close as possible and find justified values for cuts that might not be clear from a look at the real data.

These types of simulations make use of probability theory to model the physical phenomena occurring in e.g. a testbeam, where a random value is extracted from a model's probability distribution. The extraction of values can be viewed as a dice throw, where the simulation program generates a random number and extract a value from the probability distribution associated to that number.

An example may be that of a particle traversing a thin layer of silicon where we want to measure the energy loss. The probability function in this case would be the Landau distribution (Chapter 2) from which a random value is extracted.

6.1 Simulation Frameworks

6.1.1 GEANT4

In the testbeam scenario a large number of models are needed in order to simulate all the physics occurring in the beam/telescope interactions and the electron-hole mechanisms inside the silicon. This is realized through the use of the GEANT4 simulation framework.

GEANT4 is a simulation framework based upon C++ in order to simulate a

complete range of processes. This framework consists of a wide range of physical Monte Carlo models for different types of particle interactions in matter. In general the framework gives the user the ability to create a geometrical model of a detector with different materials and a large number of components, and to define sensitive areas of the geometry that record particle interactions. These sensitive areas can be chosen to be the electrodes in a pixel detector and further, the hits in these sensitive areas can be "digitized" meaning that the detector system's response to the hit is modelled. Also different types of particles have their own models. Different particles interacts through different forces thus they must be modelled separately.

In order to simulate energy loss of a particle in a material, GEANT4 divides the particle's passage into steps, where the energy loss in each step is calculated and added together when the particle has traversed the material. These steps have a certain length associated to them and the step length can be detrimental to the precision in some processes. If for instance three processes are modelled simultaneously the process that requires the smallest step size determines the step length while the other two processes get a recalculation of the probability of their phenomena occurring in each step. This method enables the simulation of ionization event throughout the doped silicon in the detectors and also the drift-diffusion mechanisms of the electron-hole pairs. Important to know is that GEANT4 only calculates the energy loss of the particles in a material based on the material type and the physical interaction that contributes to the energy loss. It does not natively simulate drift-diffusion phenomena so in order to get a detailed and correct simulation all other effects and phenomena must be programmed by the user.

Therefore, when simulating a more complex system all underlying models must be accounted for and added together in a seamless way. This can be very demanding for large simulation scenarios where several detectors and materials needs to be simulated.

6.1.2 Allpix simulation framework

The Allpix framework [40] [41] is a simulation framework placed on top of GEANT4, creating classes and macros that ease the way of simulating large scale systems such as a testbeam. It is described by its developer, Dr. Mathieu Benoit, as a generic pixel detector simulation framework, that lets the user start doing simulations much faster than by writing a new GEANT4 script from scratch. In order to set up a very basic simulation with Allpix, three scripts needs to be written or edited;

- A geometry file describing all the relevant properties of the pixel detector such as pixel pitch, pixel size, number of pixels, sensor size, pcb geometry and bump bonding layout. Also this geometry file describes the readout clock frequency

and other features of the readout electronics.

- A digitizer file which is a script that transforms the measured energy loss in the GEANT4 steps into hits in the pixels of the simulated detector. In this script several important phenomena must be modelled such as drift-diffusion, electric fields and dopant concentrations. Additionally, in this file is where one must write new functions for adding extra material to the simulation.

- The last file that is needed is the macro file. As in GEANT4 this is the file that brings the different geometries and digitizers together, as well as setting up the world and choosing how detailed the physics model should be. Basically choosing what kinds of interactions that are needed to simulate the experiment. Choosing a EM-interaction physics model only will not account for particle interactions that happens through anything other than the electromagnetic force.

Allpix simulations can be divided into three blocks where each does a specific simulation task and has different time scales associated to them. The first "block" is the Technology Computer-Assisted design (TCAD) [42] simulation. TCAD simulates the electric field in the way that it would look like in a pixel detector as well as the induced current on the electrodes (Eq. 2.15). This is a very extensive simulation and it takes hours to simulate one event. On the other hand, this simulation gives an extremely detailed map of the electric field that can be used in conjunction with properties simulated in the other two blocks.

The second block is the digitization of the system. Here charge sharing and electronics are simulated by the use of a parametric model. Meaning that the collection time, trapping time, threshold, bias etc. is treated as parameters to be determined by the user. This block makes it possible to simulate 10-100 events per second.

The third and final block is the Monte Carlo simulation of the charge transport in the detector. This block makes use of the E-field maps from the TCAD simulation, the parameters from the digitization model and the energy deposition collected from GEANT4. This gives a detailed simulation of the detector response while keeping the computing cost low and effective. This block also simulates some effects on it's own, such as drift and diffusion of charge carriers, trapping effects as a result of radiation damage and some temperature dependent fluctuations of the material and carrier properties. The model used for simulating trapping effects is a probability that is dependent on the collection time and the carrier lifetimes (Eq. 1.15).

$$P(t) = \frac{e^{t/\tau_i}}{\tau_i} \tag{6.1}$$

where t is the collection time (Eq. 2.13) and τ_i is the carrier lifetimes, with $i = n, p$. These values are set as parameters in the simulation, and is determined by the user. The drift model is simply Eq.(2.10) since the electric field have been simulated extremely detailed in TCAD.

All these blocks are written to be as generic as possible in order to simplify the simulations of large scale systems.

6.1.3 Simulation setup

The goal of the simulation in this thesis was to do a full simulation of the testbeam, where the mimosa planes, the DUTs and the telescope is simulated. This in order to get more insight into the properties of the DUTs such as how material effects (fake hits, multiple scatterings etc.) affect the resolution of the detectors, and to justify cuts that are performed in the analysis code. In Appendix I, the macro file for setting up the simulation environment is included. This file serves as the linking between the different parts that needs to come together in the simulation scenario.

First the telescope planes, the DUTs and any additional materials (cooling box, holders, mounting structures etc.) are defined in the environment. This step also allows the user to set the threshold in the detectors. Next the user initializes the simulation world by choosing the physics list, the step length for GEANT4 (mentioned above) and building the simulation world. The next few steps determine whether to use some visualization or not and control the level of feedback to the terminal after each event. The latter can be viewed as the amount of information any error message should contain. Thereafter the user can control how the particles trajectories should be drawn in the visualization, and how the data should be stored.

Allpix offers two ways to store the simulation data, either by storing it in a root file or as plain text (ASCII). In both cases ToT, deposited energy, real tracks and DUT hits are stored. Furthermore, in order to ease the process even more the ASCII files can be converted into the format used in the EUTelescope reconstruction software further minimizing the difference between simulated and real data.

The last step, in the simulation, consists of choosing what kind of particles there should be in the beam and the beam's energy, shape and position. When this is set the user chooses the amount of events wanted in the simulation and it is ready to start. Figure 6.1 shows the visualization of the simulation scenario used in this thesis.

One important remark is that the DUTs are simulated as planar pixel detectors. This is because the E-field maps have not been made for a 3D electrode layout, this means that not all properties could be simulated but the general efficiency and

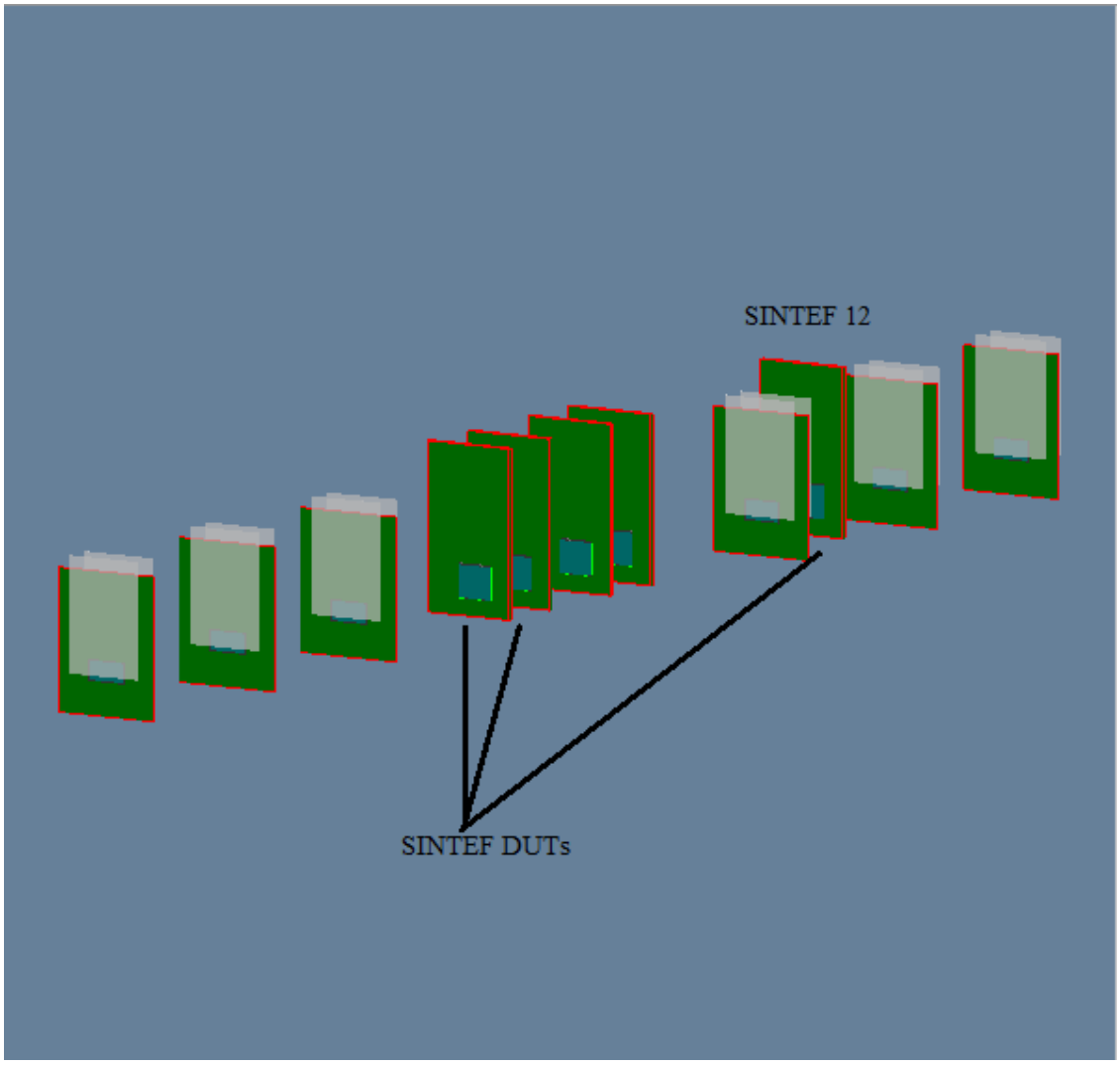

Figure 6.1: A visualization of the simulation scenario used in this thesis. The DUTs are pointed out and the grey material in front of the mimosa planes is a metallic foil. The cooling box is not simulated here.

resolutions can be compared to those of the real DUTs.

6.2 Simulation Results

During the process of setting up GEANT4 and Allpix a few important packages were missing from the online repository. One of which was a package that is a dependency of the conversion software, namely the software that converts the ASCII output into a format suitable for the EUTelescope reconstruction framework. A reconstruction script was therefore written to yield the impact points in the DUTs and the tracks from the telescope based on the simulated data. The residual plots from the alignment are shown in Figure 6.2 below.

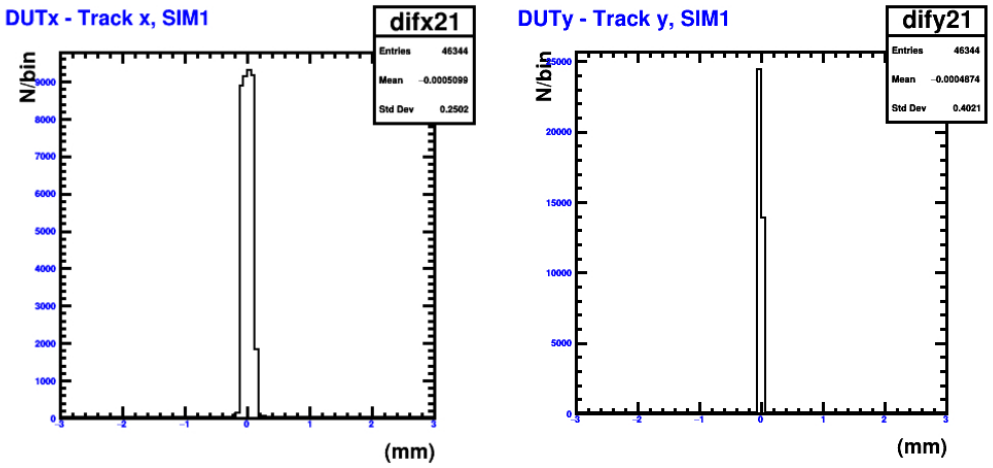

Figure 6.2: Residual plots for the simulated DUT. Sharp peak centred around 0 means we have a good alignment.

The results shown below are obtained from a simulation that contained 179 000 triggers with a threshold of 4k electrons. The tuning was set to give a ToT of 5 with a charge release of 20ke^-.

6.2.1 Clusters and Time over Threshold

As mentioned above, the results from the simulations are comparable to those of the real data. Below, in Figure 6.3 on the left the ToT distributions in the simulated DUTs are shown as well as the real DUTs ToT distributions on the right. The simulated distributions show a narrower distribution due to the lower presence of external materials and of course the parametric approach to the readout electronics. In this parametric approach to the electronics a value is set that determines the fluctuations on the signal charge. This parameter may be underestimated thus yielding a narrower distribution. The simulated distribution is, however, comparable to the ToT distribution on the right hand side with the peaks not being separated by more than approximately one ToT count.

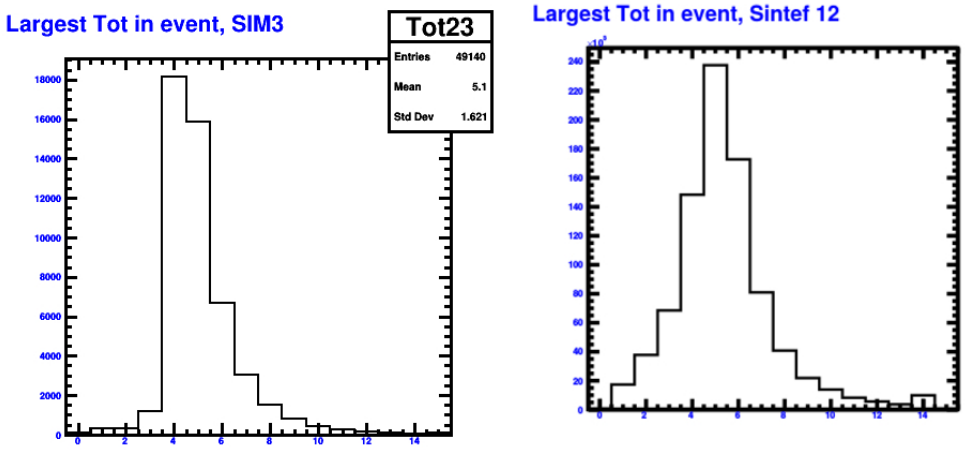

Figure 6.3: Largest ToT distributions for the DUT SINTEF 12. Left: Simulated. Right: Real.

Since the very same analysis framework is used on the simulated data the clusters are found in the same way, by identifying the largest ToT signal and add neighbouring fired pixels to the cluster. The cluster size and the cluster multiplicity distributions are shown in Figure 6.4. In these plots the peak is very sharply centred at 1, which indicates that most of the particles energy is also deposited in the seed pixel here.

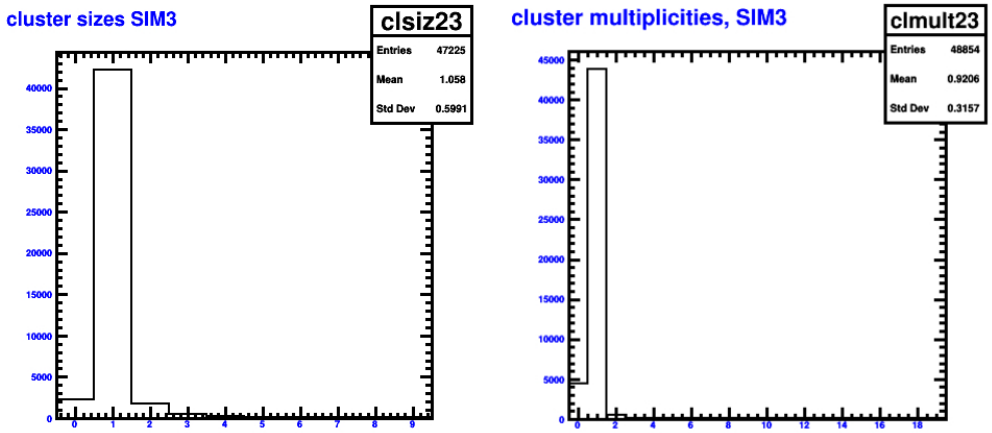

Figure 6.4: Left: Cluster size distributions Right: Cluster multiplicities distribution.

Furthermore, Figure 6.5 shows how the total cluster ToT is distributed, where we can see counts of 0 ToT. This feature is not properly understood but it could be due to one of three reasons. The first being that the simulation framework stores all energy depositions in a list, also those that fall below threshold. These hits could be propagated through the clustering algorithm and yielding a summed cluster ToT

of 0. However, if this was the case one would expect the largest ToT in event to be 0 as well, from Figure 6.3 we can see that the counts of 0 ToT as the largest in an event is very low.

The second reason could be that the clustering algorithm does not have a cutoff for ToTs that are 0. Meaning that when the algorithm searches through the pixel matrix for hits, it can find additional cluster where energy have been deposited but not enough to bring the collective charge above threshold. Hence resulting in some counts of a summed cluster ToT of 0. However, this should also be visible in the plot on the right hand side in Figure 6.4 in the form of multiple clusters. This plot show a clear peak at 1 and only about 500 counts of multiple clusters compared to the > 2000 counts of total cluster ToT at 0.

The third reason might be to some property of the detectors that have not been simulated properly in the simulation framework. Further investigation regarding this third reason is needed.

By fitting the residual plots, the resolution is acquired. The simulated detectors have very little deviation since they do not have any broken areas or damaged bump bonding associated to them. Furthermore the detectors simulated here are simulated as planar pixel detectors so no features due to the holes will be seen. This is of course not optimal but still several properties can be compared to the real data as long as one keep this in mind. Figure 6.6 show the residuals in y-direction for the simulated detector on the left and for the real detector on the right.

Figure 6.7 show the residual distributions for the simulated and the real detector in x-direction (the wide dimension of the pixels). Here it is visible that the simulated sensor does not have any electrode holes since no clear dips in the distribution is present at the platou.

In both dimensions we can see that the detectors track resolutions is comparable. In the plots of the short dimension of the pixel (y-direction) we can even see that the simulation produces a worse resolution than what is seen in the real data. This is nothing unusual and only show that the simulation actually include effects that is detrimental to the results such as multiple scattering and electronic noise.

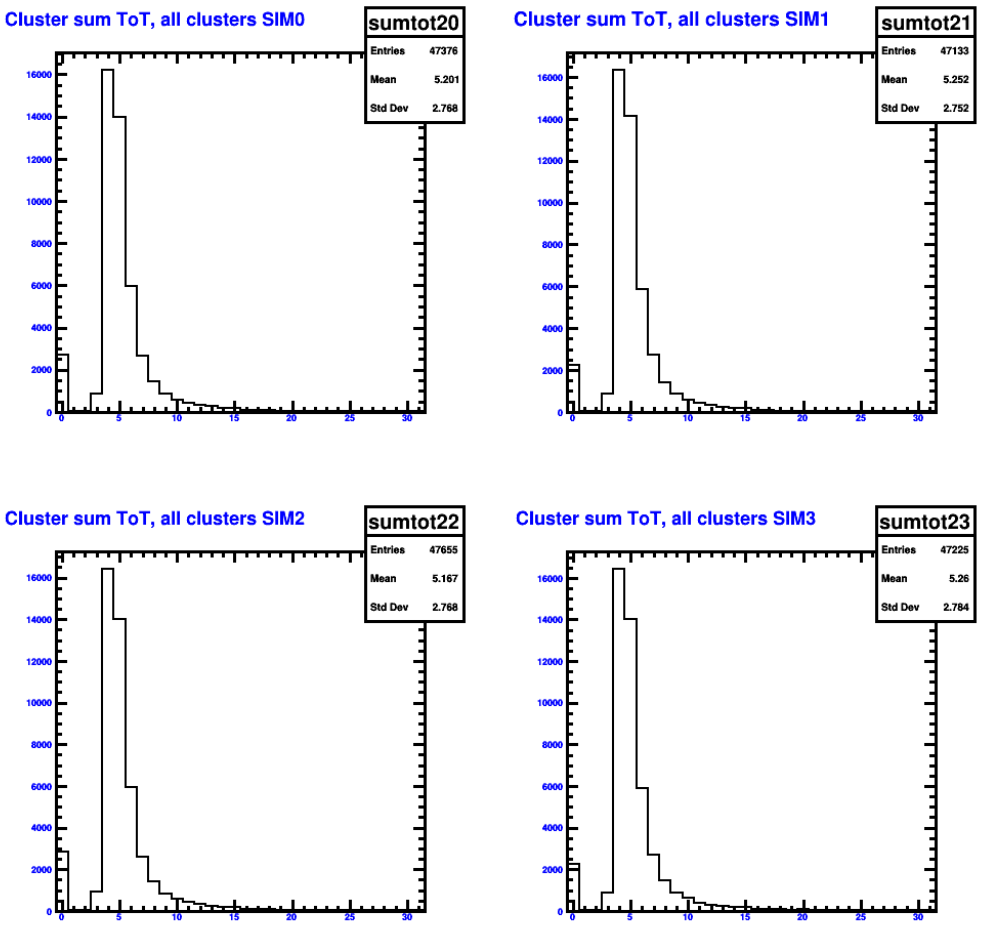

Figure 6.5: Distribution of the clusters total ToT. A small peak is visible at 0 ToT.

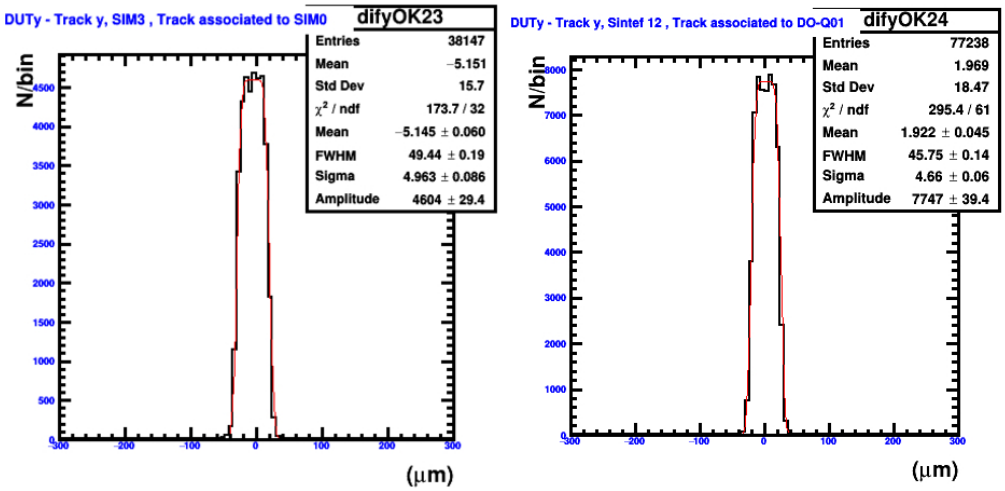

Figure 6.6: Left: Residuals in y-direction for the simulated equivalent of SINTEF 12. Right: the residuals in y-direction of the real SINTEF 12 detector.

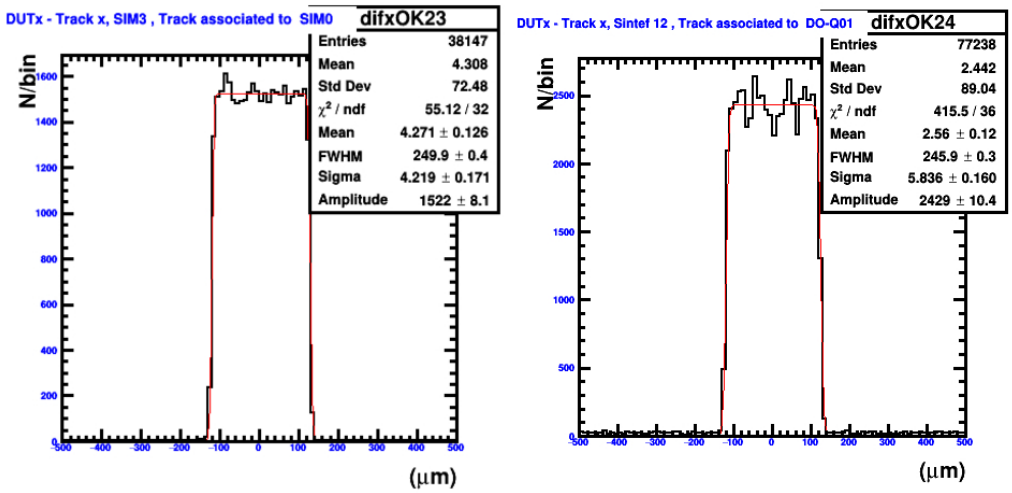

Figure 6.7: Left: Residuals in x-direction for the simulated equivalent of SINTEF 12. Right: the residuals in x-direction of the real SINTEF 12 detector.

6.2.2 Charge collection efficiency

Since the simulated sensors is planar the electrodes will not reduce the overall efficiency as they do in the real detectors. This can be seen in Figure 6.8 where all the efficiency is collected in one pixel area. Here we can see that the simulated detector have no areas with lower efficiency due to electrode "holes".

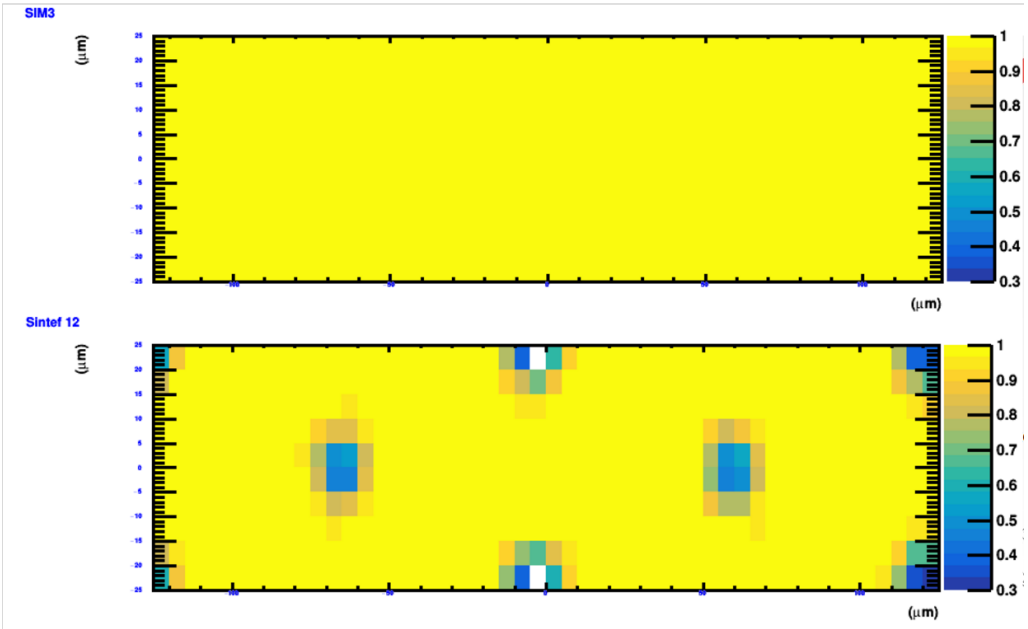

Figure 6.8: Top: Efficiency map of a simulated planar detector, showing 100% efficiency everywhere. Bottom: The real SINTEF 12 detector with clearly visible low-efficiency electrodes.

In the analysis framework the efficiency is found by applying a window shaped cut on the position that the tracks from the particles must fall within (section 5.2.3). The response of the efficiencies as a function of this window size can be of value when determining the optimal window size that yields the optimal efficiency. Obviously, having a window size that extends throughout the entire sensor area is of no use and it is of interest to keep this window as small as possible. Figure 6.9 shows the efficiencies of the real and simulated SINTEF 12 detector as a function of the window size in y-direction. The y-direction is chosen because this is the pixels short dimension and any cut here, that is too small, results in a significant change in the efficiency. Since the width of the pixels in the x-direction is larger, the cut performed for the y-direction is of greater interest.

From the figure we can see that the response to narrower window size along the pixels short dimension is comparable for both the real and the simulated data. The simulated efficiencies lies higher than the real data since the simulated detector contain no electrode holes and therefore it has no efficiency loss associated to those.

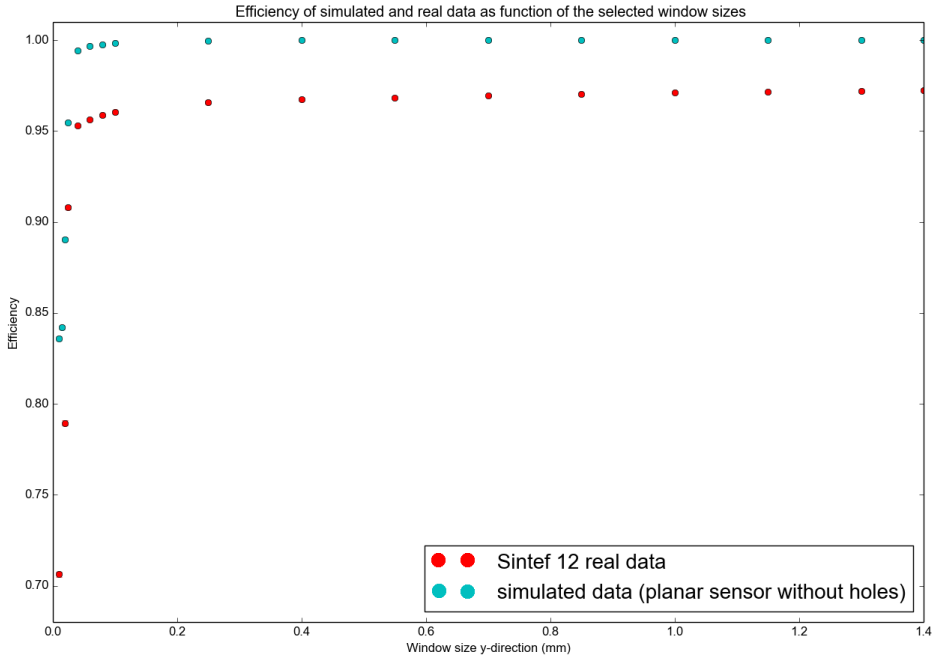

Figure 6.9: Simulated and real detector efficiencies as function of "window" cut size in the pixels short dimension.

Furthermore, the breakdown occur roughly at a window cut size approximately at the pixels width ($50\mu m$) but the real data show a slight slope before this breakdown. This slope is most likely due to the amount of material in front of the DUTs in the test beam, which is not present in the simulation scenario. More material result in more multiple scatterings and as such the efficiency (which is dependent on precise tracks) can suffer.

Figure 6.10 show the efficiency as function of window size along the y-direction for both simulated and real detector but with the efficiency of the real data normalized to the simulated. This is done in order to more clearly see the deviation in responses.

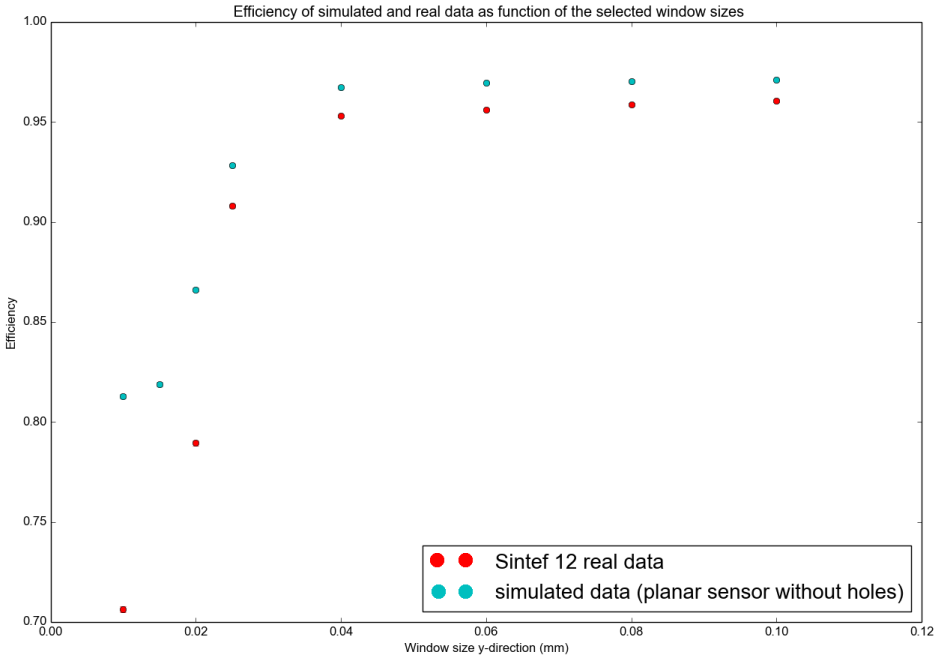

Figure 6.10: zoomed view of the efficiency as function of the window size along the y-direction. The efficiencies from the real data are normalized to the simulated one to more clearly see the differences.

From Figure (6.10) we can see that the efficiency is following approximately the same shape for simulated and real data. By the use of this plot the window size in y-direction was set to $0.15mm$, which is the point just before the rapid drop, for the efficiency analysis since this gave the best results without leaving the window too large.

Chapter 7

Conclusion and Outlook

Conclusion

An analysis framework and a Monte Carlo simulation have been developed and used to analyse several properties of 3 new silicon 3D pixel detector prototypes.

The detectors were tested in two test beams in 2015 and 2016 where in the 2016 test beam only SINTEF 12 was used. These test beams provided large amounts of useful data for efficiency studies, track resolution studies and active edge characterization. Unfortunately the irradiated SINTEF 11 detector broke down before it could be tested, and as such no radiation hardness studies have been performed. However, the IV characteristics of the detectors were measured during the 2015 test beam and showed that full depletion is obtained at approximately 5V bias voltage. Additionally these curves showed that SINTEF 10 had a very large leakage current and thus was excluded from further testing in 2016.

The tracking resolution studies showed good results for all detectors and especially for SINTEF 12. Furthermore, the efficiency of SINTEF 12 was measured to be above 97%.

In the 2016 test beam the SINTEF 12 detectors active edge were investigated. The results from the analysis showed that the active edge extends beyond the nominal edge of the sensor, and that this extension is different in the short and long dimensions of the pixels. However, the conclusion is that the active edge is functioning with a high charge collection efficiency.

A full Monte Carlo simulation of the test beam experiment have been performed where the results were comparable to those of the test beam analysis. Further work regarding the implementation of this 3D electrode layout as well as including more

detailed materials in the simulation is needed. This is because the simulation did not include the 3D electrode geometry of the detectors and a planar geometry was instead used.

Outlook

A new 3D pixel detector prototype is being designed and manufactured by UiO and SINTEF respectively, and is expected to be finished in 2017. This new prototype utilizes a new readout chip (RD53) [43] as well as a new electrode layout [44]. Test beams studies regarding the properties of these detectors will be performed once they are finished. The framework and simulation developed for this thesis may prove helpful when such a study would be performed, although a few implementations is still missing in the simulation.

In the simulation framework, the electric field between the electrodes needs to be simulated very detailed in TCAD. This is very demanding, and have not been performed yet. However, a solution that does not need a TCAD simulation is to take the efficiency maps from the test beams and apply them to the simulation. This would effectively implement inefficiencies due to the electrodes by associating the hit map of the simulated DUT, to the efficiency map of the real data.

Bibliography

[1] Burkhard Schmidt. The high-luminosity upgrade of the lhc: Physics and technology challenges for the accelerator and the experiments. *Journal of Physics: Conference Series*, 706(2):022002, 2016.

[2] Philip Hofmann. *Solid State Physics: An introduction*. Wiley-VCH Verlag & Co., 2013.

[3] Charles Kittel. *Introduction to solid state physics, 8th edition*. John Wiley & sons, inc., 2005.

[4] Dr. William R. Leo. *Techniques for Nuclear and Particle Physics Experiments: A how-to approach*. Springer-Verlag, 2nd edition, 1994.

[5] Ben G. Streetman and Sanjay Kumar Banerjee. *Solid State Electronic Devices*. Pearson Prentice Hall, Pearson Education Inc., 6th edition, 2006.

[6] Kevin F. Brennan. *The physics of semiconductors: With applications to optoelectronic Devices*. Cambridge university press., 1999.

[7] The bonding structure of undoped silicon. `http://iamtechnical.com/bonding-structure-undoped-silicon`, accessed 22.03.2017.

[8] Nöel SERVAGENT. Semiconductor sensors and applications. `http://www.optique-ingenieur.org/en/courses/OPI_ang_M05_C02/co/Contenu.html`, accessed 03.05.2017.

[9] Helmuth Spieler. *Semiconductor Detector Systems*. Oxford University Press Inc., 2014.

[10] Physics figures. `http://users-phys.au.dk/philip/pictures/physicsfigures/physicsfigures.html`, accessed 31.05.2017.

[11] J. Lange et. al. 3d silicon pixel detectors for the high-luminosity lhc. *Journal of Instrumentation*, 11(11):C11024, 2016.

[12] A. Gligorova et al. Comparison of planar and 3d silicon pixel sensors used for detection of low energy antiprotons. http://bora.uib.no/bitstream/handle/1956/9610/Comparison_IEEE.pdf;jsessionid=AE2F25DD5791811F58DC6B97FB648371.bora-uib_worker?sequence=3, accessed 01.06.2017.

[13] FEI4 Collaboration. The fe-i4b integrated circuit guide. https://wiki.physics.hawaii.edu/pub/Main/BeastTechnicalDocumentation/FE-I4B_V2.0.pdf, accessed 31.05.2017.

[14] Håvard Gjersdal. *Test beam track reconstruction and analysis of ATLAS 3D pixel detectors*. PhD thesis, University of Oslo, 2014.

[15] Tesfaye Ayalew. *SiC semiconductor devices technology, modeling, and simulation*. PhD thesis, Technischen Universität Wien, Fakultät für Elektrotechnik und Informationstechnik, 2004.

[16] Stefano Meroli. Radiation damage for silicon detectors. http://meroli.web.cern.ch/meroli/lecture_radiation_damage_silicon_detector.html, accessed 18.04.2017.

[17] Konrad Kleinknecht. *Detectors for Particle Radiation*. Cambridge University Press, 2nd edition edition, 1998.

[18] Interactions of charged particles with matter. http://mtdevans.com/projects/physics-problems/interactions-of-charged-particles-with-matter/, accessed 18.04.2017.

[19] Stefano Meroli. The straggling function. energy loss distribution of charged particles in silicon layers. http://meroli.web.cern.ch/meroli/lecture_stragglingfunction.html, accessed 05.04.2017.

[20] T. Rohe N. Wermes L. Rossi, P. Fischer. *Pixel Detectors From Fundamentals to Applications*. Springer-Verlag, 2006.

[21] PD Yoder, K Gärtner, and W Fichtner. A generalized ramo–shockley theorem for classical to quantum transport at arbitrary frequencies. *Journal of Applied Physics*, 79(4):1951–1954, 1996.

[22] Ramo-shockley theorem. Lecture slides for students in Instrumentation. Berkley Lab. Given 05.03.2015. https://indico.physics.lbl.gov/indico/event/285/material/slides/0?contribId=1, accessed 29.05.2017.

[23] Glen Cowan. Error analysis for efficiency. https://www.pp.rhul.ac.uk/~cowan/stat/notes/efferr.pdf, July 2008.

[24] P La Rocca and F Riggi. The upgrade programme of the major experiments at the large hadron collider. *Journal of Physics: Conference Series*, 515(1):012012, 2014.

[25] CERN. The accelerator complex. `https://home.cern/about/accelerators`, accessed 21.04.2017.

[26] Science and Technology Facilities Council. Cern accelerator complex. `http://www.stfc.ac.uk/research/particle-physics-and-particle-astrophysics/large-hadron-collider/cern-accelerator-complex/`, accessed 03.05.2017.

[27] Bruno Muratori Werner Herr. Concept of luminosity. `https://cds.cern.ch/record/941318/files/p361.pdf`, accessed 25.04.2017.

[28] Alejandro Garcia Ernest M. Henley. *Subatomic Physics*. World Scientific Publishing Co. Pte. Ltd, 3rd edition edition, 2007.

[29] `http://homepages.physik.uni-muenchen.de/~Otmar.Biebel/MDT-Photos/ATLAS-Detektorschema.gif`, accessed 26.04.2017.

[30] The ATLAS Collaboration. Atlas detector and physics performance technical design report. `https://cds.cern.ch/record/391176/files/cer-0317330.pdf`, accessed 01.06.2017, may 1999.

[31] T. Flick. The phase ii atlas pixel upgrade: the inner tracker (itk). *Journal of Instrumentation*, 12(01):C01098, 2017.

[32] Erik J. Ramberg. ILCWS08 Test Beam Summary. In *Linear colliders. Proceedings, International Linear Collider Workshop, LCWS08, and International Linear Collider Meeting, ILC08, Chicago, USA, Novermber 16-20, 2008*, 2009.

[33] AIDA 2020 programme. Overview of testbeams, digital image. `http://aida2020.web.cern.ch/content/cern`, accessed 03.05.2017.

[34] J. Baudot et al. First test results of mimosa-26, a fast cmos sensor with integrated zero suppression and digitized output. *2009 IEEE Nuclear Science Symposium Conference Record (NSS/MIC)*.

[35] Hendrik Jansen et al. Performance of the eudet-type beam telescopes. *EPJ Techniques and instrumentation*, 2016.

[36] Homepage of eutelescope framework collaboration. `http://eutelescope.web.cern.ch/`, accessed 29.05.2017.

[37] I. Rubinsky. Eutelescope offline track reconstruction and dut analysis software. `https://www.eudet.org/e26/e28/e86887/e107460/EUDET-Memo-2010-12.pdf`, accessed 29.03.2017.

[38] Louis Lyons. *Statistics for nuclear and particle physicists*. Cambridge University Press, 1992.

[39] Burton DeWilde. 3d silicon pixel sensors: Recent test beam results. `file:///home/ahe122/Downloads/iWorid2010%20(2).pdf`, accessed 09.05.2017, 2010. Powerpoint presentation at 12th international workshop on radiation imaging detectors.

[40] Mathieu Benoit. The allpix simulation framework twiki page. `https://twiki.cern.ch/twiki/bin/viewauth/Main/AllPix`, accessed 31.05.2017.

[41] Mathieu Benoit. Allpix github page. `https://github.com/ALLPix/allpix`, accessed 31.05.2017.

[42] Webpage, `https://www.synopsys.com/silicon/tcad.html`, accessed 31.05.2017.

[43] N. Demaria et. al. Recent progress of rd53 collaboration towards next generation pixel read-out chip for hl-lhc. *Journal of Instrumentation*, 11(12):C12058, 2016.

[44] Gian-Franco Dalla Betta. small pitch 3d devices, presentation at the vertex 2016 conference. `https://indico.cern.ch/event/452781/contributions/2297522/attachments/1344742/2028102/Small_pitch_3D_GFDB_WEB.pdf`, accessed 31.05.2017, September 2016.

Appendices

Appendix I

```
#########################################################################
#### Telescope planes ####
#### EUD0 ####
#########################################################################
# Al Holder
/allpix/extras/setTestStructureType 8
/allpix/extras/setTestStructurePosition 0.0 0.0 0.0 mm
/allpix/extras/setTestStructureRotation 0.0 0.0 0.0 deg
/allpix/extras/setTestStructureDetLink 300
# Mimosa detector
/allpix/det/setId        300
/allpix/det/setPosition  0.0 0.0 0.0 mm
/allpix/det/setRotation  0.0 180.0 180.0 deg
/allpix/det/setLowTHL    13. keV
#########################################################################
#### EUD1 ####
#########################################################################
# Al Holder
/allpix/extras/setTestStructureType 8
/allpix/extras/setTestStructurePosition -0.227617950928 -0.254617514893 120.0 mm
/allpix/extras/setTestStructureRotation -0.0 -0.0 0.00070544 deg
/allpix/extras/setTestStructureDetLink 301
# Mimosa detector
/allpix/det/setId        301
/allpix/det/setPosition   0.1 0.1 120.0 mm
/allpix/det/setRotation   0.0 180.0 180.0 deg
/allpix/det/setLowTHL    13. keV
#########################################################################
#### EUD2 ####
#########################################################################
# Al Holder
/allpix/extras/setTestStructureType 8
/allpix/extras/setTestStructurePosition -0.492158130371 -0.17583204793 240.0 mm
/allpix/extras/setTestStructureRotation -0.0 -0.0 0.0032635 deg
/allpix/extras/setTestStructureDetLink 302
```

```
# Mimosa detector
/allpix/det/setId        302
/allpix/det/setPosition  0.2 0.2 240.0 mm
/allpix/det/setRotation  0.0 180.0 180.00 deg
/allpix/det/setLowTHL    13. keV
#########################################################################
#### EUD3 ####
#########################################################################
# Al Holder
/allpix/extras/setTestStructureType 8
/allpix/extras/setTestStructurePosition -0.871765687988 -0.135744687646 649.0 mm
/allpix/extras/setTestStructureRotation -0.0 -0.0 -0.004538 deg
/allpix/extras/setTestStructureDetLink 303
# Mimosa detector
/allpix/det/setId        303
/allpix/det/setPosition   0.3 0.3 649.0 mm
/allpix/det/setRotation   0.0 180.0 180.0 deg
/allpix/det/setLowTHL    13. keV
#########################################################################
#### EUD4 ####
#########################################################################
# Al Holder
/allpix/extras/setTestStructureType 8
/allpix/extras/setTestStructurePosition -0.98985583252 -0.170630609912 776 mm
/allpix/extras/setTestStructureRotation -0.0 -0.0 -0.0044567 deg
/allpix/extras/setTestStructureDetLink 304
# Mimosa detector
/allpix/det/setId        304
/allpix/det/setPosition  0.4 0.4 776 mm
/allpix/det/setRotation  0.0 180.0 180 deg
/allpix/det/setLowTHL    13. keV
#########################################################################
#### EUD5 ####
#########################################################################
# Al Holder
/allpix/extras/setTestStructureType 8
/allpix/extras/setTestStructurePosition -1.05242432983 -0.220215597607 896.0 mm
/allpix/extras/setTestStructureRotation -0.0 -0.0 0.0034919 deg
/allpix/extras/setTestStructureDetLink 305
# Mimosa detector
/allpix/det/setId        305
/allpix/det/setPosition  0.5 0.5 896.0 mm
/allpix/det/setRotation  0.0 180.0 180.0 deg
/allpix/det/setLowTHL    13. keV
#########################################################################
```

```
#########################################################################
#### DUT 0 ####
#########################################################################
/allpix/det/setId        200
/allpix/det/setPosition   -3.75 1.0 360.0 mm
/allpix/det/setRotation   0.0 180.0 180.00 deg
/allpix/det/setLowTHL     4. keV
#########################################################################
#### DUT 1 ####
#########################################################################
/allpix/det/setId        201
/allpix/det/setPosition   -3.75 1.0 400.0 mm
/allpix/det/setRotation   0.0 180.0 180.00 deg
/allpix/det/setLowTHL     4. keV
#########################################################################
#### DUT 2 ####
#########################################################################
/allpix/det/setId        202
/allpix/det/setPosition   -3.75 1.0 460.0 mm
/allpix/det/setRotation   0.0 180.0 180.00 deg
/allpix/det/setLowTHL     4. keV
#########################################################################
#### DUT 3 ####
#########################################################################
/allpix/det/setId        203
/allpix/det/setPosition   -3.75 1.0 500.0 mm
/allpix/det/setRotation   0.0 180.0 180.00 deg
/allpix/det/setLowTHL     4. keV
#########################################################################
#### DUT 4 ####
#########################################################################
/allpix/det/setId        204
/allpix/det/setPosition   -3.75 1.0 690.0 mm
/allpix/det/setRotation   0.0 180.0 180.00 deg
/allpix/det/setLowTHL     4. keV
#########################################################################

#########################################################################
####Extra Metrials####

#/allpix/extras/setTestStructureType 10
#/allpix/extras/setTestStructurePosition 0.0 0.0 600.0 mm

#########################################################################
```

```
#########################################################################
# Scintillators
#/allpix/eudet/scint1Pos 0.0  0.0  -24.0 mm # offset of 18mm +/- 6mm with of scinti
#/allpix/eudet/scint2Pos 0.0  0.0  -18.0 mm

#########################################################################
# Build detectors
#/allpix/phys/Physics LIVERMORE_FTFP_BERT
/allpix/phys/Physics emstandard_opt0
/allpix/det/setMaxStepLengthSensor 2 um
/run/initialize
/allpix/det/update

#########################################################################
# Verbose control
/run/verbose 0
/control/verbose 0
/control/saveHistory
/tracking/verbose 0
/allpix/phys/verbose 0

#########################################################################
# Visualization
/vis/scene/create
#/vis/scene/add/axes 0. 0. 0. 10. cm
/vis/scene/add/volume World -1 2
/vis/viewer/set/style s
#/vis/open OIX 1024x768-100+100
#/vis/open OGLIXm 1024x768-100+100
#/vis/open RayTracer
#/vis/open OGLIQt
#/vis/open OGLSQt
#/vis/open OIX
#/vis/open OGLIX 1024x768-100+100
#/vis/open OGLSXm
#/vis/open DAWNFILE
#/vis/open OGLSX
#/vis/open OGL 600x600-0+0
/vis/viewer/set/background 0.4 0.5 0.6
/vis/viewer/set/viewpointThetaPhi 20 50
/vis/viewer/zoom 2.0
/vis/viewer/flush

#########################################################################
# Draw trajectories at end of event, showing trajectory points as
# markers of size 2 pixels
```

```
/vis/scene/add/trajectories
/vis/modeling/trajectories/create/drawByCharge
/vis/modeling/trajectories/drawByCharge-0/default/setDrawStepPts false
/vis/modeling/trajectories/drawByCharge-0/default/setStepPtsSize 2
/vis/scene/endOfEventAction accumulate

#########################################################################
# Write Telescope files
/allpix/timepixtelescope/setFolderPath Run_workshop3
/allpix/timepixtelescope/setEventIDcolumn 0
/allpix/timepixtelescope/setSumTOT 1
/allpix/timepixtelescope/write 1

#########################################################################
# Write ROOT File
#/allpix/WriteROOTFiles/write 1
#/allpix/WriteROOTFiles/setFolderPath Testbeam/run5

#########################################################################
# Source GPS
/gps/particle pi-
/gps/pos/type Beam
/gps/pos/sigma_r 5.0 mm
/gps/pos/centre 1.0 2.5.0 0.0 mm
/gps/direction  0 0 1

/gps/ene/type User
/gps/hist/type energy
# spectra
/gps/hist/point 120000 1

/gps/source/list

# Source GPS
#/gps/particle mu+
#/gps/pos/centre 0 0 -1.0 mm
#/gps/direction  0 0 1

#/gps/ene/type User
#/gps/hist/type energy
# spectra
#/gps/hist/point 200000 1



#########################################################################
```

```
# Shoot
/allpix/beam/frames 100000
/allpix/beam/type const 1
/allpix/beam/on
```